Environmental Technology & Innovation 42 (2026) 104943

Contents lists available at ScienceDirect

Environmental Technology & Innovation

journal homepage: www.elsevier.com/locate/eti

A novel carbonation washing strategy for the ultrafine fraction of incineration bottom ash under wastewater reuse conditions

Meissem Mezni [a,b], Quentin Wehrung [a,c,*], Davide Bernasconi [d], Enrico Destefanis [c], Caterina Caviglia [c], Nadia Curetti [c], Federico Pasero [c], Giovanna Antonella Dino [c], Salah Mezlini [b], Fabien Michel [a], Alessandro Pavese [c], Linda Pastero [c,e]

[a] Alkaline Technologies SAS, Nantes 44700, France
[b] University of Monastir, National Engineering School of Monastir (ENIM), Mechanical Engineering Laboratory LR99ES32, Monastir 5019, Tunisia
[c] Earth Science Department, Università degli Studi di Torino, Torino 10125, Italy
[d] Centre for Engineering Research, University of Hertfordshire, Hatfield, United Kingdom
[e] NIS-Nanomaterials for Industry and Sustainability Inter-departmental centre, Università degli Studi di Torino, Torino 10135, Italy

ARTICLE INFO

Keywords:
Municipal solid waste incineration bottom ash
Carbonation washing
Water reuse
Secondary cementitious materials

ABSTRACT

Municipal solid waste incineration bottom ash (IBA) ultrafine fractions (< 0.25 mm) exhibit high leaching potential, limiting their reuse despite their suitability for mineral valorization. This study evaluates a carbonation washing strategy under water reuse conditions to stabilize these fractions while enabling their use as supplementary cementitious materials (SCMs) and reducing CO_2 emissions and water demand. A total of 13 laboratory-scale experiments were conducted in a 1 L stirred reactor equipped with a porous stone sparger, treating 1.3 kg of IBA ultrafines. Potentially toxic elements (PTEs) were monitored in both recycled process water and carbonated solids. Carbonation washing induces a strong reduction in leaching for most regulated elements after a single treatment step (up to −95% for Pb, −93% for Cu, −85% for Ni, −71% for Cd, −67% for As and −78% for Cl^-). In contrast, increased leaching was observed for a limited number of species, notably Cr (+16%), Sb (+171%) and SO_4^{2-} (+108%). With increasing cycle number, partial re-enrichment occurs due to solute accumulation in the recirculated water; however, after 13 cycles, all metals except Sb remain below French Type 1 and Type 2 thresholds. Cr exhibits a distinct behaviour, with leaching decreasing across cycles and falling below the Type 1 limit from cycle 8 onward. The process achieves stable CO_2 uptake on the order of 100 gCO_2/kg IBA, unaffected by increasing salinity and metal accumulation in the recycled water. Water recovery efficiencies of approximately 88% per cycle were maintained, with dissolved species approaching asymptotic concentrations controlled by secondary phase precipitation. Overall, carbonation washing provides substantial stabilization of IBA ultrafines and constitutes a relevant process building block for their treatment, although the increased mobility of specific species, particularly Sb and SO_4^{2-}, indicates that further process optimization is required.

* Corresponding author at: Alkaline Technologies SAS, Nantes 44700, France.
E-mail address: quentin.wehrung@unito.it (Q. Wehrung).

https://doi.org/10.1016/j.eti.2026.104943
Received 10 February 2026; Received in revised form 31 March 2026; Accepted 19 April 2026
Available online 20 April 2026

1. Introduction

1.1. Background and context

The incineration of municipal solid waste (MSW) remains a central component of waste management strategies across Europe, offering continuous waste disinfection, significant volume reduction, and partial energy recovery (Sun et al., 2016). In France, 126 MSW incineration facilities were in operation in 2024, illustrating the sector's enduring prominence within national waste-to-energy infrastructures (Beylot et al., 2018; Dong et al., 2018; Julcour et al., 2025; Kleib et al., 2021). Yet, the alignment of incineration with long-term sustainability and circular economy objectives remains debated (Zou et al., 2025). Challenges related to carbon emissions, limited material recovery, long-term release of potentially toxic elements (PTEs), and end-of-process management highlight the need for advanced residue treatment pathways (Vehlow et al., 2007; Dou et al., 2017; Fletcher and Dunk, 2023). In this context, improving the environmental performance and resource recovery potential of incineration residues has become a key priority to ensure the long-term sustainability of waste-to-energy systems.

Among these residues, incineration bottom ash (IBA) constitutes the largest solid residue stream, representing 20–25 wt% of the incoming waste. In the EU, an estimated 7–8 Mt of IBA fines (< 2 mm) are produced each year, of which approximately 1 Mt originates from France (Blasenbauer et al., 2020). IBA is a highly heterogeneous, mineral–metal assemblage composed of silicates, aluminosilicates, glasses, metallic inclusions, and various Ca- and Al-bearing hydration phases inherited from combustion and post-combustion conditions (Bayuseno and Schmahl, 2010; Wei et al., 2011). Within this matrix, the fine fraction (IBA fines), commonly defined as particles < 2 mm, and particularly those < 0.25 mm, plays a critical role in determining environmental performance (Huber et al., 2019). Although IBA ultrafines < 0.25 mm generally account for only 8–15 wt% of fresh IBA, they exhibit the highest leachability, reactivity, and surface-controlled dissolution rates owing to their elevated specific surface area and enrichment in soluble salts (Buchholz and Landsberger, 1995; Caviglia et al., 2019; Destefanis et al., 2020; Mantovani et al., 2021, 2023). Consequently, IBA ultrafines simultaneously represent:

- a waste management challenge, due to elevated concentrations and release potentials of potentially toxic elements (PTEs) such as Cu, Zn, Pb, Ni, Cr, Sb, and Mo, often exceeding reuse thresholds; and
- an opportunity, as their high reactivity makes them particularly suitable for accelerated mineral carbonation, with the potential to stabilize contaminants and mineralize substantial quantities of CO_2.

As a result, controlling the behaviour of this ultrafine fraction is critical, as it disproportionately governs bulk IBA leaching and ultimately constrains large-scale reuse pathways.

1.2. Characteristics and challenges of IBA ultrafines

Currently, after 3–9 months of bulk ageing, followed by screening and metal recovery, IBA is primarily used in low-value applications such as road sub-base aggregates and geotechnical fills (Asal et al., 2019; Spreadbury et al., 2021; Hyks et al., 2025; Shen et al., 2025). State-of-the-art separation technologies, mainly overband magnets and eddy current separators, remain notoriously inefficient at recovering metals contained in the fine fraction (Šyc et al., 2020). Thus, it is well established that oxide-bound and microparticulate metals largely remain unrecovered (Allegrini et al., 2014; Xia et al., 2017; Nørgaard et al., 2019; Zhang et al., 2025). As a consequence, an estimated 2.14 Mt of base, strategic, critical, and precious metals are downcycled each year across the EU, including Al, Cu, Zn, Sn, Cr, Pb, Sb, Ag, and Au. This loss comprises approximately 1.0 Mt of mineral fraction and 0.97 Mt of ferrous materials, largely associated with untreated bottom ash, as well as ~0.18 Mt of non-ferrous metals, primarily originating from unrecovered IBA (Bruno et al., 2021).

The mineralogical assemblage of IBA fines includes reactive calcium-aluminate hydrates such as hydrocalumite (Friedel's salt, Hcl, $Ca_4Al_2(OH)_{12}Cl_2{\cdot}4\ H_2O$), ettringite (Ett, $Ca_6Al_2(SO_4)_3(OH)_{12}{\cdot}26\ H_2O$), and Ca-rich gels, along with traces of portlandite ($Ca(OH)_2$) (Alam et al., 2019a). These phases exhibit high reactivity in presence of dissolved CO_2 (Baciocchi et al., 2010; Um et al., 2013; Cheng et al., 2025). Their dissolution–precipitation dynamics form stable carbonate products, mainly calcite and Mg-calcite ($Ca_{1-x}\ Mg_x\ CO_3$), thereby promoting both CO_2 uptake and the immobilization of certain ions by coprecipitation (Yeo et al., 2024). Such characteristics make the IBA fines an attractive feedstock for accelerated aqueous carbonation technologies (ACT), particularly when treatment aims to improve environmental quality while supporting low-carbon material valorization.

1.3. Carbonation washing and wet processing approaches

Carbonation washing, recently proposed as a direct aqueous treatment for highly reactive residues such as air pollution control residues (APCr), integrates mineral carbonation with contaminant removal in a single process step (Wehrung et al., 2024a). The approach relies on promoting extensive particle dissolution under CO_2-rich conditions and coupling this dissolution with the extraction of soluble PTEs into a process water. In this study, we extend this concept to IBA ultrafine fraction, which presents distinct mineralogical features, lower chloride contents than APCr, and a markedly different dissolution/carbonation behaviour. Unlike APCr, whose reactivity is driven largely by lime additions in the flue gas cleaning train, the reactivity of IBA ultrafines derives primarily from the abovementioned hydration products formed during combustion, quenching, and weathering, as well as from Ca- and Mg-silicate matrices susceptible to partial dissolution under mildly acidic carbonation conditions. Although APCr contains higher alkali contents, this work focuses on IBA ultrafines within emerging wet processing strategies in Europe aimed at enabling reuse under increasingly

stringent regulations. In this context, once the material is processed in the aqueous phase, it is advantageous to couple washing, CO_2 mineralization, and metal recovery within an integrated treatment framework.

A key challenge in implementing washing techniques at scale is water management (Caviglia et al., 2022; Chen et al., 2023; Bansal et al., 2024; Bernasconi et al., 2025). High liquid-to-solid ratios (L/S) enhance dissolution and CO_2 absorption but generate large volumes of contaminated wastewater. To reduce water consumption and move toward a circular water strategy, process waters can be recirculated across consecutive carbonation batches. However, such recirculation leads to the progressive accumulation of PTEs and salts, which may influence dissolution kinetics, carbonation efficiency, PTE partitioning, and ultimately the environmental safety of the carbonated solids. Designing robust, scalable treatment schemes therefore requires a precise understanding of how PTEs accumulate in the liquors, under what conditions accumulation becomes limiting, and when make-up water or partial purge streams become necessary.

1.4. Research gap and objectives

Despite increasing interest in wet processing and carbonation-based treatments, the behaviour of such systems under wastewater recirculation remains insufficiently understood, particularly with respect to PTE accumulation, process stability, and long-term operability. Accordingly, this study aims to provide a process-oriented and quantitative assessment of carbonation washing applied to IBA ultrafines (< 0.25 mm) under controlled water reuse conditions. Relying on the methodology established for APCr, we adapt the process to the geochemical features of IBA ultrafines, with an emphasis on quantifying PTE accumulation patterns and assessing their implications for system design. The work was conducted within the framework of the ASHES program (Advanced Sampling for a Harmonized Environmental Solution), an academia–industry collaboration between the Earth Sciences Department of the University of Turin (Italy) and Alkaline Technologies SAS (France) (Wehrung et al., 2025a). In this context, the objectives of the present study are to:

1. Characterize the carbonation behaviour of IBA ultrafines under wastewater reuse conditions, including CO_2 absorption rate and uptake;
2. Quantify the accumulation of PTEs and major ions in the recirculated wastewater, identify elements of concern, and evaluate their evolution over cycles;
3. Assess the implications of wastewater composition for the leachability of carbonated IBA ultrafines, in view of regulatory thresholds and circular-economy valorization pathways (e.g., low-carbon binders);
4. Provide engineering-relevant insights into optimizing recirculation strategies, determining when intervention (purges, dilution, or polishing) is required, and guiding the design of integrated treatment systems for IBA fine fractions.

Overall, this work demonstrates how carbonation washing, when coupled with engineered wastewater recirculation, can serve as a high-efficiency treatment step for stabilizing fine IBA fractions, reducing water consumption, and supporting their integration into

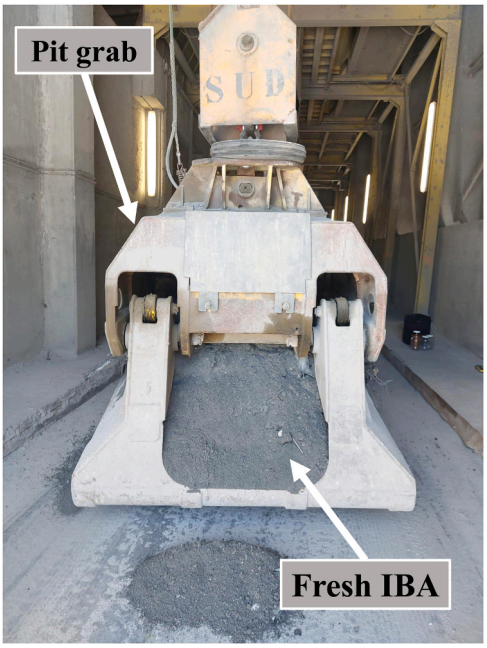

Fig. 1. Pit grab filled with fine, fresh IBA during sample collection at the waste-to-energy (WtE) plant.

advanced circular material cycles. Beyond fundamental insights, the results provide quantitative data to support process design, scale-up, and environmental compliance in emerging mineral carbonation-based treatment systems.

2. Materials and methods

2.1. Reagents, and bottom ash samples sourcing and preparation

CO_2 (99.9% purity) was supplied by Sapio. Ultrapure, degassed water was used in all experiments. A bulk batch of about 10 kg of incineration bottom ash (IBA) was collected from a representative municipal solid waste (MSW) incineration plant located in the Auvergne–Rhône–Alpes region (southeastern France). The facility is authorized to process approximately 180,000 tons of MSW annually. Sampling was carried out directly in the IBA pit, from a heap located beneath the conveyor belt immediately after quenching. As illustrated in Fig. 1, the ash was collected using the facility's pit grab. The material was transferred directly from the grab into airtight containers, sealed on site, then oven-dried at 105 °C during 24 h.

The dried ash was subjected to dry sieving so as to separate the ultrafine fraction (< 0.25 mm) from coarser fractions. A total of 1.365 kg of ultrafines was obtained, corresponding to 15.7 wt% of the sieved sample. The coarser fractions (> 0.25 mm) were retained for investigations outside the scope of the present study. The particle size distribution of the bulk IBA prior to sieving was characterized by cumulative mass percentages of 15.7, 23.4, 37.0, 54.7, 78.3, and 100 wt% passing 0.25, 0.5, 1, 2, 4, and 10 mm sieves, respectively, indicating a substantial contribution of fine particles within the raw material.

2.2. Experimental procedures

The experimental setup for the aqueous carbonation tests is shown in Fig. 2. A 1.5 L double-walled Pyrex reactor was used, equipped with gas flow sensors, a mechanical stirrer (AM20-D, ArgoLab), and connected to a thermostatic bath. To ensure the gas flow sensors were properly calibrated, multiple "blank" experiments were carried out. During these calibrations, a linear relationship was observed between the flow measurements at the valve and those at the flow meter, resulting in $FLOW\_BLANK_{valve} = k_{cal} \cdot FLOW\_BLANK_{flow\ meter}$.

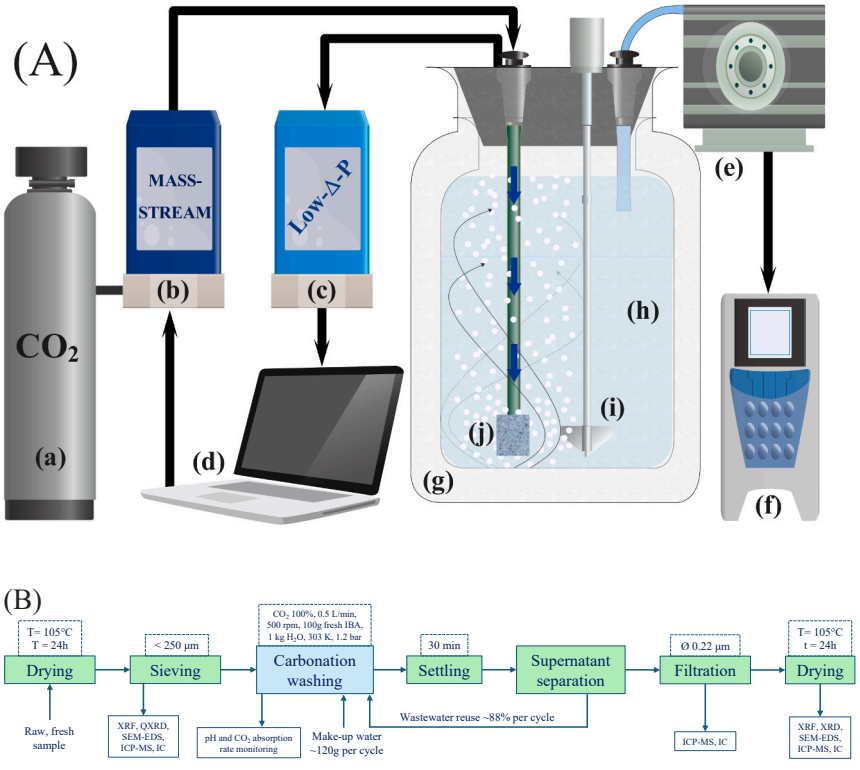

Fig. 2. (A) Modular experimental setup for carbonation washing experiments. The bold blue and thin black arrows indicate the CO_2 flow. (a) gas tank; (b) valve; (c) flow meter; (d) computer with remotely adjustable control settings for gas flow sensors; (e) peristaltic pump; (f) pH/EC meters; (g) double-wall Pyrex reactor; (h) IBA aqueous suspension; (i) mechanical stirrer equipped with a variable-frequency drive for adjustable rpm; (j) porous stone sparger. Adapted with permission from (Wehrung et al., 2024b). (B) Experimental procedure with detailed operational parameters.

2.2.1. Carbonation washing

Ten replicate NF EN 12457–2 (AFNOR, 2002) leaching tests were performed on fresh IBA ultrafine samples (< 0.25 mm) to establish baseline concentrations of salts and metals. The reported values correspond to the average of these replicates and are referred to as the R_i sample. Carbonated solid samples are labelled A1–A13, corresponding to successive carbonation washing cycles (cycle 1–13). The associated process waters, collected directly from the reactor at the end of each cycle, are labelled C1–C13. Leachates obtained from the carbonated solids according to NF EN 12457–2 are therefore denoted A1–A13, each A_i corresponding to the leaching test performed on the solid produced during cycle *i*, and each C_i to the corresponding process water of the same cycle.

Thirteen experimental runs were performed, corresponding to as many consecutive cycles under water reuse conditions (experiments C1–C13). The number of carbonation washing cycles was selected to capture early-cycle non-linear trends as well as extended operation for assessing process resilience. In this respect, Electrolytical Conductivity (EC, μS/cm) increased during the initial cycles and subsequently reached a plateau, indicating that the recirculated process water approached saturation with respect to highly soluble salts, primarily SO_4^{2-} and Cl^-. Beyond this point, further cycles were not expected to provide additional insight.

In each run, 100 g of IBA were mixed with 1 L of water (L/S = 10). This relatively high L/S ratio was selected to limit the rapid saturation of the liquid phase and to better resolve pollutant release, accumulation, and stabilization mechanisms during carbonation washing. In addition, an L/S ratio of 10 enables direct comparison of the resulting wastewaters with NF EN 12457–2 batch leaching tests. The suspension was transferred into the reactor and stirred at 500 rpm for at least 10 min to ensure homogeneity, under N_2 atmosphere to prevent from premature carbonation with ambient air. Prior to starting, CO_2 was flushed through the reactor at 2 L/min via a top inlet to remove residual air. At t = 0, CO_2 was introduced through a porous stone sparger at the reactor bottom at 303 K, a flow rate of 0.5 L/min and a pCO_2 of 1.2 bar, generating micro-bubbles that are known to enhance mineral carbonation kinetics, as set out in Table 1 (Jiang et al., 2024).

Each experiment was interrupted when the flow meter indicated a near-zero CO_2 uptake, in combination with a solution pH in the range 7 < pH < 8. Upon completion, 10 mL of the solution were withdrawn directly from the reactor through a 0.22 μm syringe filter. Two diluted subsamples were prepared: one for IC and one for ICP-MS, the latter acidified with HNO_3. Final pH and EC were measured.

The remaining suspension was allowed to settle for 30 min to separate the supernatant from the solid residue, which was then collected by filtration through a 0.45 μm membrane. To maintain a constant liquid mass (1 kg), ultrapure water was added before recycling the recovered supernatant for the subsequent experiment.

2.3. Analytical methods

2.3.1. In-situ monitoring of CO_2 uptake by gas flow sensing

CO_2 flows and total CO_2 uptake were controlled and measured by a Bronkhorst modular system, composed of: Mass Stream ("valve" hereafter) (MFC D-6321), with a maximum flow range of 2 Ln/min CO_2 and accuracy ± 1.0% RD plus ± 0.5% FS; low ΔP ("flow meter" hereafter) F101E (max flow range of 3 Ln/min CO_2 and accuracy ± 1.0% FS). A digital pc-board provides self-diagnostics, alarm and counter functions, digital communication (RS232), remotely adjustable control settings, and an on-board interface based on the FLOW-BUS protocol makes it possible to communicate via a multi-bus system. CO_2 flow rate acquisition data was performed every 1 s.

2.3.2. Scanning electron microscopy with Energy-dispersive X-ray spectroscopy

Scanning Electron Microscopy (SEM) imaging was performed using a TESCAN VEGA equipped with a tungsten (W) filament and both secondary electron (SE) and backscattered electron (BSE) detectors. The images presented in this study were typically acquired using the BSE detector, with an accelerating voltage of 10 kV, a beam current of 30 pA, a working distance of 6 mm. Elemental microanalysis was carried out using an Xplore 15 Energy-Dispersive X-ray Spectroscopy (EDXS) detector (Oxford Instruments, Abingdon, UK), operated via AZtecONE software and integrated with the SEM in both SE and BSE modes. IBA ultrafine samples were mounted on circular aluminium stubs (10 mm diameter, 3 mm height) using double-sided conductive carbon adhesive tape. The powders were gently tapped to remove loosely bound particles and then lightly pressed using a clean surface to ensure adequate fixation. Prior to analysis, the samples were C-coated.

2.3.3. X-ray powder diffraction

X-Ray Powder Diffraction (XRPD) measurements were carried out using a Rigaku MiniFlex 600 benchtop X-ray diffractometer (Bragg-Brentano geometry, CuKα radiation, X-ray source operating at 600 W (40 kV, 15 mA); D/teX Ultra silicon strip detector; 5° < 2θ < 80°, step width 0.02°, scan speed 0.1°/min). Quantitative phase analysis (QXRPD) was performed by Rietveld refinement using TOPAS-Academic and the fundamental parameters approach. Powdered samples (~5 g) were homogenized and finely ground using zirconium ball milling. An aliquot of approximately 1 g was then mixed with 10 wt% high-purity corundum as an internal standard for amorphous content estimation and placed in a standard sample holder, ensuring a flat and homogeneous surface to minimize preferred

Table 1
Detailed experimental parameters for the experiments with their corresponding identifiers.

Exp. ID	Description	IBA	H_2O	L/S	CO_2 flow	Temperature	pCO_2	Stirring	Completion criterion
		g	kg	–	L/min	K	bar	rpm	–
C1–C13	Water reuse cycles	100	1	10	0.5	303	1.2	500	pH 7–8 & CO_2 absorption rate < 5%

orientation effects.

2.3.4. X-ray fluorescence

The elemental composition of the original and carbonated IBA samples was determined by X-ray Fluorescence (XRF; Rigaku Supermini200). For analysis, samples were mixed with LicoWax binder at a 12:1.5 mass ratio and pressed into 4 cm diameter pellets under 15 tons of hydraulic pressure. The balance, corresponding to the unidentified components (mainly CO_2 and H_2O), was also provided by the instrument. Loss on Ignition (LOI) measurements, performed by firing the samples at 1473 K, confirmed that the balance closely matched the LOI values, with a deviation within ±0.5 wt%.

2.3.5. Leaching tests

Leaching tests were performed according to the European standard EN-12457–2, involving deionized water and particles with diamater < 4 mm at a liquid-to-solid ratio of 10. Tests were conducted before and after treatment to compare leachate concentrations of chemical species with the legal limits for IBA reuse set by French regulations (Directeur général de la prévention des risques, 2011; Blasenbauer et al., 2020). The corresponding French thresholds for reuse compliance (Type 1 and Type 2) are reported in Table S1.

2.3.6. Ion chromatography

Ionic Chromatography (IC) analysis was performed by a Metrohm 883 Basic IC plus equipped with an autosampler (863 Compact) and an anion column (Metrosep A Supp 4 – 250/4.0). The detected ions were fluoride, chloride, sulfate, nitrate, phosphate, and bromide.

2.3.7. Inductively coupled plasma–mass spectrometry

Inductively Coupled Plasma–Mass Spectrometry (ICP–MS) (Thermo Fisher iCAP-TQe coupled to ASX 560 autosampler) was used to quantify Al, As, Cd, Cu, Co, Cr, Fe, Mn, Ni, Pb, Sb, and Zn in wastewaters collected from carbonation washing experiments. Samples were filtered, diluted with ultrapure water, and acidified to 0.1% v/v with HNO_3 High Purity grade. Calibration was performed using five standards ranging from 1 to 50 mg/L.

2.3.8. pH, EC, and mass measurements

pH and EC (electrolytical conductivity, μS/cm) of the samples were measured by a Hanna HI H-ORP meter and a Mettler Toledo Five Easy EC-meter, respectively. The sample masses were measured with a relative precision of ±0.01% and an absolute accuracy of ±0.1 g.

2.4. Data treatment

The CO_2 absorption rate as a function of time $\eta(t)$ (%) was determined by measuring the influent and effluent CO_2 volumetric flow with the valve and the flow meter, placed at the reactor inlet and outlet, respectively. In doing so, the instantaneous absorption rate as a function of time was measured, according to the equation below (Eq. 1):

$$\eta(t) = 100 \times \left(1 - \frac{k_{cal} \bullet \mu(t)}{B(t)}\right) \tag{1}$$

where $B(t)$ (L/min) = Valve recording of the in-flow; $\mu(t)$ (L/min) = Flow meter recording of the out-flow; k_{cal}: calibration factor as defined in the above section. Note that $\eta(t)$ includes the fractions of CO_2 that are either mineralized or dissolved into the active solution.

The average CO_2 absorption rate over the interval of time $[t_1, t_2]$, $\overline{\eta_i}$ (%), was defined as followed (Eq. 2):

$$\overline{\eta_i} = \frac{\sum_{t_1}^{t_2} \eta(t)}{n} \tag{2}$$

where $[t_1, t_2]$ = interval of time for which $\overline{\eta_i}$ is being calculated; n = size of the studied sample of $\eta(t)$ values.

In addition to $\eta(t)$, V_{CO2} (L), the volumetric CO_2 uptake during the interval of carbonation time $[t_1, t_2]$, was introduced (Eq. 3):

$$V_{CO_2} = \int_{t_2}^{t_1} \eta(t') \bullet B(t')\, dt \tag{3}$$

In this work, the theoretical carbonation capacity φ representing the maximum theoretical amount of CO_2 (gCO_2/kg_{IBA}) that can be stored by accelerated carbonation was calculated with the difference between the modified Steinour equation and the mass of CO_2 inherently present as $CaCO_3$ (Eq. 4) (Chang et al., 2015):

$$\varphi\ (gCO_2/kg_{IBA}) = \frac{M_{CO_2}}{100} \bullet \left(\alpha \frac{CaO}{M_{CaO}} + \beta \frac{MgO}{M_{MgO}} + \gamma \frac{SO_3}{M_{SO_3}} + \delta \frac{P_2O_5}{M_{P_2O_5}}\right) \bullet 10^3 - \quad m_{CO_2} \tag{4}$$

where CaO, MgO, SO_3 and P_2O_5 (wt%) = Elemental concentrations of Ca, Mg, S and P, expressed as oxides, obtained by XRF; M_x (g/

mol) = Molar mass of those oxides; α, β, γ *and* δ = pH-dependents coefficients factoring the relative contribution of each oxide such as in an IBA aqueous system; $\alpha = \beta = 1; \gamma = -1; \delta = -2$ were chosen based on the IBA-CO_2-water system chemistry (Renforth, 2019); m_{CO_2} = mass of CO_2 inherently present as $CaCO_3$, quantified using Rietveld refinement.

The degree of carbonation achieved ω (gCO_2/kg_{IBA}), calculated from the perfect gas equation, was determined as follows:

$$\omega\ (gCO_2/kg_{IBA}) = \frac{P * V_{CO_2} * M_{CO_2}}{R * T} * \frac{1000}{m_i} \tag{5}$$

where $P(Pa)$ = operating pressure; $V_{CO_2}\ (m^3)$ = volume of CO_2 absorbed by the active suspension, determined with the gas flow sensors; $M_{CO_2}\ (g \bullet mol^{-1})$ = CO_2 molar weight, $R(J \bullet mol^{-1} \bullet K^{-1})$ = perfect gas constant; $T(K)$ = operating temperature; m_i (g) = initial IBA sample mass, before carbonation experiment.

The carbonation efficiency ε (%) reflects the effectiveness in harnessing the carbonation potential of the material as follows:

$$\varepsilon \quad (\%) = \frac{\omega}{\varphi} \bullet 100 \tag{6}$$

The water recovery efficiency α (%), defined as the average percentage of water mass recovered per carbonation cycle under wastewater reuse conditions, was finally calculated as follows:

$$\alpha\ (\%) = 100 - \frac{\sum_{c_1}^{c_i} \left(\frac{m_0 - m_{f,i}}{m_0} \bullet 100\right)}{n_i} \tag{7}$$

where m_0 (kg) = Initial mass of water during the carbonation washing test (constant) = 1.2 kg; $m_{f,i}$ (kg) = Mass of supernatant recovered after the carbonation washing test of cycle *i*; n_i= number of carbonation washing and supernatant separation cycles.

3. Results and Discussion

3.1. Physicochemical characterization of the raw IBA ultrafines

3.1.1. Morphology, microstructure and microanalysis

Fig. 3 shows the visual comparison between the raw IBA and the carbonated product, highlighting a shift from a pale beige powder to a slightly darker beige-grey material. This difference likely reflects the progressive transformation of the mineral assemblage during carbonation, including the dissolution of light-colored hydrocalumite-type phases and the concomitant formation of microsized calcite. Fig. 4 illustrates the SEM–EDS analyses of characteristic phases in the raw IBA.

Fig. 4 presents the SEM–EDS observations of characteristic phases identified in the raw IBA < 0.25 mm. The overview micrograph (Fig. 4a) shows the highly heterogeneous nature of the ultrafines, composed of angular to subrounded particles spanning from sub-micron debris to ~50–100 μm fragments. This matrix, typical of ultrafine IBA, comprises intermixed silicate particles, porous Ca–aluminate hydrates, metallic inclusions, and oxide grains (Speiser et al., 2000; Wei et al., 2011; Loginova et al., 2019).

Overall, the IBA ultrafines shows an abundance of metallic oxides, the most common being Zn-oxide particles (Fig. 4c), Fe-oxide particles occurring as flat, elongated rough fragments with hematite- or magnetite-like compositions (Fig. 4d), and Ba–Ti–rich spherical to subrounded grains (Fig. 4e). Traces of base-metal–bearing particles, including Cu-, Sn-, Ni- and Pb-rich grains, were also detected.

Au-rich grains were detected (Fig. 4F), exhibiting a sharp BSE contrast and a compact metallic habit. The occurrence of gold particles in the < 0.25 mm fraction is well documented, typically originating from the fragmentation of jewellery, electronic circuitry, or Au-plated components, with their abundance varying depending on the waste source (Muchova et al., 2009; Morf et al., 2013; Beikmohammadi et al., 2023; Chuchro et al., 2025)

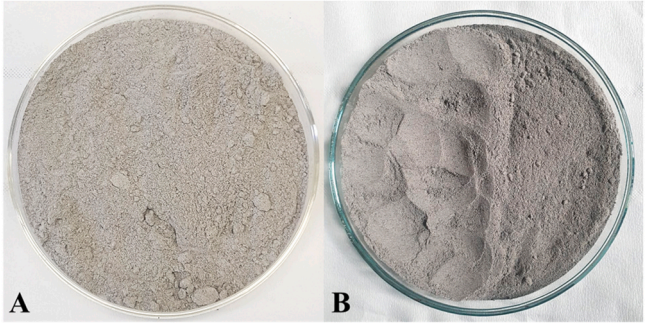

Fig. 3. Qualitative comparison of the samples: (A) raw IBA, exhibiting a light beige–grey powder, and (B) carbonated IBA, showing a slightly darker beige-grey tone. On image B, the left side is slightly packed.

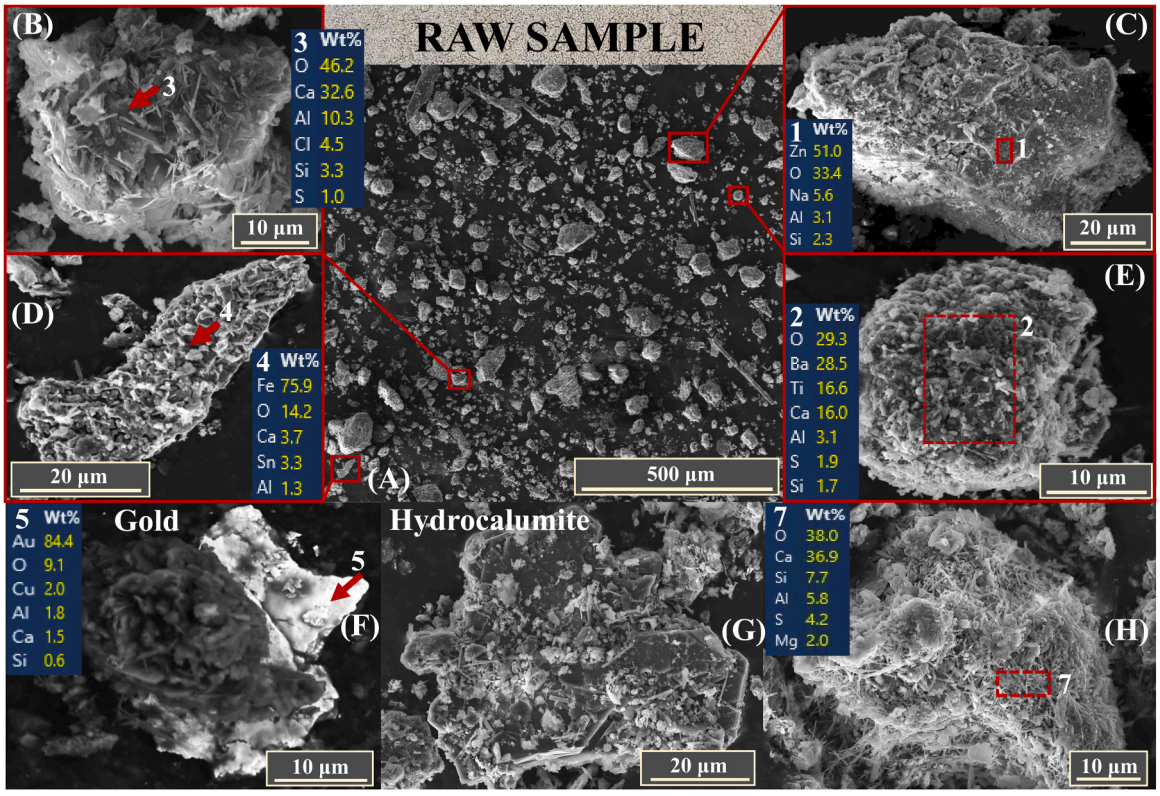

Fig. 4. SEM–EDS patterns of characteristic phases and minerals observed in the raw IBA (< 0.25 mm). (A) Overview of the sample. Metallic and oxide phases: (B) hydrocalumite, (C) zinc oxide, (D) iron oxide, (E) barium–titanium oxide, (F) BSE image of gold, (G) hydrocalumite, (H) ettringite-rich assemblage.

The ultrafine matrix contains abundant Ca–Al hydrates, particularly hydrocalumite (Hcl, Friedel's salt). In Figs. 4b and 4g, Hcl occurs as platy to foliated aggregates with intergrown lamellar microstructures; in Fig. 4g, the characteristic hexagonal habit of Hcl is clearly distinguishable. EDS spectra are dominated by Ca, Al and O, with minor Cl and S, consistent with mixed Cl–SO_4 AFm compositions commonly reported in Hcl formed in Cl- and SO_4-rich environments (Um, 2019; Matsumoto and Takaoka, 2021).

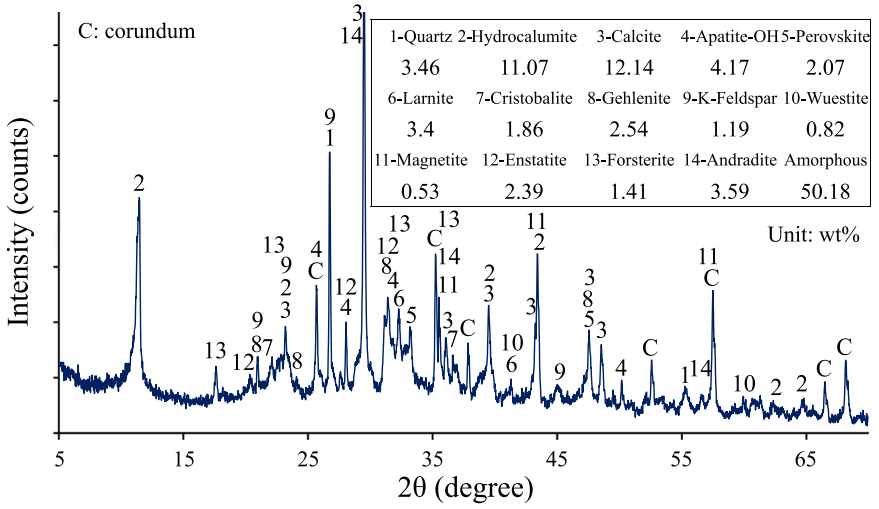

Fig. 5. XRPD pattern of raw IBA with Rietveld quantification. C denotes corundum, added as an internal standard at 10 wt%. Identified crystalline phases include: quartz (SiO_2), hydrocalumite ($Ca_4Al_2(OH)_{12}Cl_2{\cdot}4\,H_2O$), calcite ($CaCO_3$), hydroxyapatite ($Ca_5(PO_4)_3OH$), perovskite ($CaTiO_3$), cristobalite ($SiO_2$), larnite ($\beta$-$Ca_2SiO_4$), gehlenite ($Ca_2Al(AlSiO_7)$), K-feldspar ($KAlSi_3O_8$), wüstite (FeO), magnetite (Fe_3O_4), enstatite ($MgSiO_3$), forsterite (Mg_2SiO_4), andradite ($Ca_3Fe_2(SiO_4)_3$), together with an amorphous fraction.

A second family of Ca-aluminate hydrates consists of elongated needle-like acicular crystals forming loosely bound clusters (Fig. 4H). The morphology and Ca–Al–Si–S–rich composition suggest an ettringite-rich assemblage, consistent with reported morphologies in IBA (Speiser et al., 2000).

3.1.2. Mineralogy and chemistry

Fig. 5 shows the XRPD pattern of the raw IBA sample together with the Rietveld refinement quantification. The crystalline assemblage is dominated by Ca–Al and Ca–Si bearing phases, accompanied by secondary silicates, oxides, minor carbonates, and substantial amorphous fraction (~50 wt%). Hydrocalumite ($Ca_4Al_2(OH)_{12}Cl_2{\cdot}4\ H_2O$, 11.1 wt%) and larnite (β-Ca_2SiO_4, 3.4 wt%) were identified as the most potentially reactive Ca-bearing phases, while calcite ($CaCO_3$, 12.1 wt%) and quartz (SiO_2, 3.5 wt%) were also identified. Other constituents include hydroxylapatite ($Ca_5(PO_4)_3OH$, 4.2 wt%), perovskite ($CaTiO_3$, 2.1 wt%), gehlenite ($Ca_2Al(AlSiO_7)$, 3.4 wt%), K-feldspar ($KAlSi_3O_8$, 1.2 wt%), cristobalite (1.9 wt%), wüstite (FeO, 0.8 wt%), magnetite (Fe_3O_4, 0.5 wt%), enstatite ($MgSiO_3$, 2.4 wt%), forsterite (Mg_2SiO_4, 1.4 wt%) and andradite ($Ca_3Fe_2(SiO_4)_3$, 3.6 wt%), together with a substantial amorphous fraction (~50 wt%). This mineral assemblage is consistent with compositions typically reported for IBA fine fractions in the literature, comprising (i) residual phases (e.g., quartz), (ii) incineration-derived phases (melilitic slags and iron oxides), and (iii) quenching and weathering products such as calcite, ettringite, gypsum, and hydrous Fe- and Al-oxides (Yin et al., 2011; Wei et al., 2011; Inkaew et al., 2016; Keber et al., 2020; Alam et al., 2019b; Kasina et al., 2024).

The carbonation potential of hydrocalumite and larnite can be expressed by the following stoichiometric reactions (Eq. 8 and Eq. 9) (Wehrung et al., 2024c, 2025b):

$$2[Ca_2Al(OH)_6Cl \bullet 2H_2O] + 3CO_2(g) = 3CaCO_3(s) + Al_2O_3 \bullet xH_2O(s) + CaCl_2(aq) + (10 - x)H_2O(l) \quad (8)$$

$$Ca_2SiO_4 + 2CO_2(g) = 2CaCO_3(s) \quad + SiO_2(s) \quad (9)$$

Considering stoichiometry and the measured mineral proportions, the complete conversion of hydrocalumite and larnite alone would yield ~63 gCO_2/kg of IBA, highlighting their dominant role in the reactivity of this sample. It is expected, however, that more stable phases such as gehlenite, enstatite, forsterite and andradite, as well as amorphous Ca- and Mg-rich fractions, may provide a minor additional contribution to carbonation.

Bulk chemical composition determined by XRF (Table 2) confirms the prevalence of CaO (32.9 wt%), Al_2O_3 (12.1 wt%) and SiO_2 (11.8 wt%) as major constituents. Significant concentrations of P_2O_5 (2.2 wt%), SO_3 (3.3 wt%) and Cl (1.4 wt% in atomic form) reflect the presence of phosphates, sulfates and chlorides, while Fe_2O_3 (2.7 wt%) and MgO (2.5 wt%) account for Fe- and Mg-bearing silicates and oxides. The measured loss on ignition (26.5%) is largely attributable to CO_2 release from pre-existing carbonates and structural hydroxyl groups.

Applying Eq. 4 (modified Steinour equation), the overall oxide composition yields a theoretical carbonation capacity (φ) of 199.5 gCO_2/kg IBA. This value substantially exceeds the ~63 gCO_2/kg IBA associated with the identified hydrocalumite and larnite fractions, highlighting the additional contribution expected from amorphous and less soluble crystalline phases.

Table S2 presents the distribution of major elements between the crystalline and amorphous fractions of the raw IBA, as derived from combined XRF and XRPD analyses. The results indicate that a large proportion of certain elements is hosted in the amorphous phase, notably Ca (59%), Al (73%), and K (73%), while Si is predominantly bound in crystalline phases (~88%). Importantly, nearly 59% of the total Ca is associated with the amorphous fraction, suggesting that a significant part of the carbonation potential may arise from poorly ordered Ca-bearing phases in addition to the crystalline phases identified above.

3.1.3. Leaching behaviour of the raw samples

Fig. 6 reports: (i) leaching concentrations of metals and salts in the raw sample (histograms A and B); and

(ii) leaching concentrations together with pH and EC of the carbonated samples as a function of the carbonation cycle number (panels C–N). For the n^{th} cycle, the carbonation-inducing solution consists of the wastewater recovered from the previous $(n–1)^{th}$, and reflects the wastewater reuse strategy adopted in this study. The complete dataset of metal concentrations and physical-chemical parameters for all NF EN 12457–2 leachates (A1–A13) and carbonation wastewaters (C1–C13) is reported in Table S3, while IC-measured anion concentrations are provided in Table S4.

In this work, the results are analyzed with respect to the French limit thresholds for the reuse of IBA in road sub-base applications, as defined by the NF EN 12457–2 leaching test (Type 1 and Type 2 classifications, Table S1). Type 1 corresponds to materials used in sub-base layers up to 3 m high for sidewalks or paved road shoulders. Type 2 corresponds to embankments for infrastructure works or covered road structures, with permitted heights up to 6 m.

It is important to emphasize that the grain-size fraction investigated in this study (< 0.25 mm) is significantly finer than the fraction

Table 2
Chemical composition of raw IBA ultrafines, determined by XRF and expressed in wt% of oxides. Chloride (Cl) is also included, expressed in atomic form. The loss on ignition (LOI) is expressed as a percentage.

Oxide	Na_2O	MgO	Al_2O_3	SiO_2	P_2O_5	SO_3	Cl	K_2O	CaO	TiO_2	Cr_2O_3
wt%	1.32	2.45	12.10	11.84	2.24	3.33	1.44	0.76	32.91	1.23	0.079
MnO	Fe_2O_3	NiO	CuO	ZnO	Rb_2O	SrO	ZrO_2	BaO	PbO	SnO_2	LOI
0.106	2.671	0.016	0.164	0.495	0.004	0.071	0.014	0.151	0.046	0.026	26.532

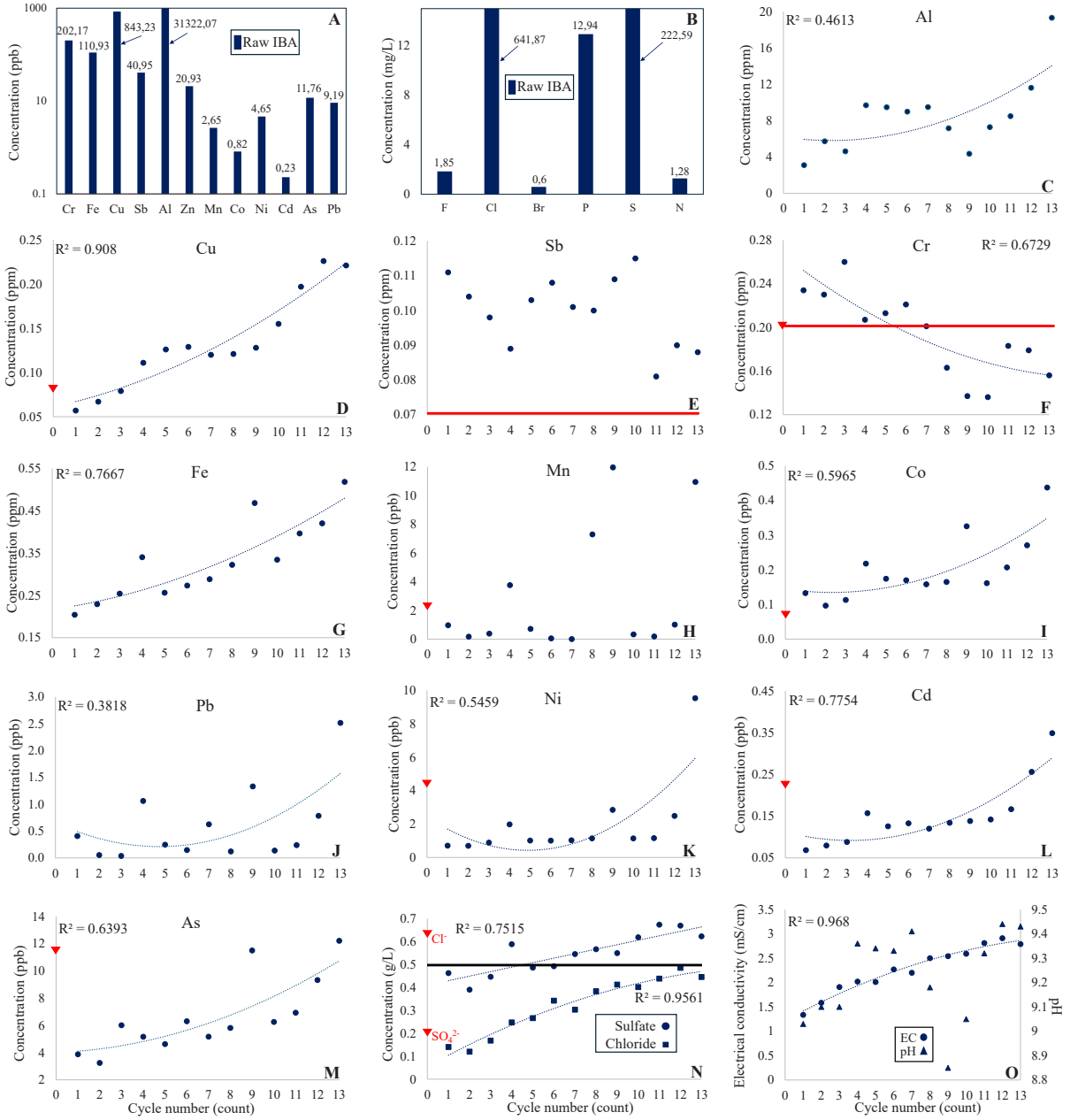

Fig. 6. Panels (A) and (B) show the average fresh samples (R_i) NF EN 12457–2 leaching concentrations for metals and salts, respectively. Panels (C)–(M) report the leaching concentrations of the carbonated samples (A1–A13) for: (C) aluminum, (D) copper, (E) antimony, (F) chromium, (G) iron, (H) manganese, (I) cobalt, (J) lead, (K) nickel, (L) cadmium, and (M) arsenic. Panels (N) and (O) present sulfate and chloride leaching concentrations and the corresponding EC/pH values. The red and black horizontal lines indicate the French regulatory limit values for Type 1 and Type 2 reuse, respectively. Type 2 limits are more restrictive than Type 1 and are therefore set at higher concentrations, in most cases above the upper bound of the plotted range. For sulfate and chloride, Type 1 and Type 2 limits are identical. Where both limit lines are not shown, the corresponding concentrations are well below the applicable thresholds and thus fall outside the graphical range. Red triangles represent leaching concentrations of the pre-carbonation samples. The absence of a triangle indicates that pre-carbonation leaching concentrations were substantially higher than those measured after carbonation and thus lie outside the plotted range, except for Sb, for which leaching increases after carbonation.

for which these regulatory limits are defined (< 4 mm). As such, particular attention is required when interpreting these results, since this ultrafine material exhibits a maximum reactive surface area and, consequently, the highest leaching potential of the whole IBA matrix. Therefore, achieving leaching concentrations that only slightly exceed regulatory thresholds for this isolated ultrafine fraction implies that, once formulated with a binder, the resulting solidified material is likely to comply with the limit thresholds.

EC and pH in the leachates of the raw samples consistently range from 3.35 to 4.05 mS/cm and from 11.42 to 11.48, respectively.

The chloride and sulfate concentrations range from 595 to 735 mg/L and 170–311 mg/L, respectively. The corresponding regulatory thresholds are 1000 mg/L (Type 1) and 500 mg/L (Type 2). Therefore, chloride leaching systematically exceeds the limit for reuse in Type 2 applications, while sulfate concentrations remain compliant with both application types. These chloride levels are consistent with those reported for IBA fines, where leachable Cl typically spans several hundred mg/L and is mainly governed by highly soluble salts such as halite, as well as by the decomposition of Cl-bearing layered double hydroxides (e.g. Hcl) under weathering or carbonation conditions (Um, 2019; Alam et al., 2020). In contrast, sulfate concentrations frequently approach or exceed reuse thresholds for IBA, due to their association with pH-sensitive phases such as gypsum or ettringite (Chrysochoou and Dermatas, 2006; Chen et al., 2023). Overall, the present Cl and SO_4^{2-} leaching ranges are consistent with commonly reported concentrations for raw IBA, confirming chloride and sulfates as primary limiting species for reuse.

Chromium (Cr) concentrations range from 150 to 250 μg/L, exceeding the Type 1 limit in two out of three cases and systematically exceeding the Type 2 limit. These leaching levels are higher than those commonly reported for MSW IBA in NF EN 12457–2-type tests, where Cr concentrations are generally lower, largely because most literature studies focus on coarser BA fractions (< 4 mm) (Um et al., 2013). In contrast, the ultrafine fraction investigated here (< 250 μm) exhibits a much higher specific surface area and reactivity, which promotes Cr release under alkaline leaching conditions.

Antimony (Sb) concentrations (28–57 μg/L; Type 2 threshold: 60 μg/L) fall within the range commonly reported in the literature and are consistent with Sb being a recurrent controlling element for IBA reuse. While remaining below regulatory limits, Sb levels are frequently reported to approach threshold values, particularly for fine fractions, reflecting the persistence and pH sensitivity of Sb-bearing phases such as Romeite $Ca_2Sb_2O_6(O,OH)$ (Cornelis et al., 2006, 2008; Verbinnen et al., 2017; Vogel et al., 2024). Fluoride (F^-) concentrations (1.2–2.2 mg/L) remain compliant but are relatively close to the Type 2 limit of 3 mg/L. All other measured elements are well below the regulatory limits. Copper (Cu) ranges from 740 to 943 ppb, nickel from 3.7 to 6.0 ppb, lead from 6.6 to 13.0 ppb, cadmium from 0.17 to 0.28 ppb, and arsenic from 7.2 to 15.4 ppb, all far below their respective thresholds. Zinc, not reported in Fig. 6, is either not detected or present at very low concentrations (≤ 21 ppb), also well within regulatory compliance.

Overall, the measured leaching concentrations are consistent with those reported in the literature, although high variability is observed, with occasional peaks in elements such as Cu, Zn, Ni, Mo, V, among others (Gori et al., 2011; Santos et al., 2013; Di Gianfilippo et al., 2016, 2018; Alam et al., 2017).

3.2. Carbonation washing performances under wastewater reuse conditions

3.2.1. CO_2 absorption rate and total uptake

Thirteen carbonation washing and supernatant separation cycles were performed under wastewater reuse conditions. Fig. 7 illustrates the evolution of the CO_2 absorption rate patterns ($\eta(t)$), while Table 3 summarizes the mean absorption rate $\overline{\eta}(t)$, maximum absorption rate $\eta(t)_{max}$ with standard deviation σ, carbonation step duration, volumetric CO_2 uptake V_{CO2}, carbonation degree achieved ω, final EC and pH for each cycle C1-C13.

The results show that $\eta(t)$ was consistently sustained across cycles, with only transient decreases during individual runs. Importantly, $\eta(t)$ systematically returned to comparable levels at the onset of subsequent cycles, indicating that the progressive accumulation of ions in the recycled solution did not impair the absorption kinetics. On average, the mean absorption rate reached 17.6%, with $\eta_{max}(t)$ values exceeding 40%.

Most cycles were intentionally interrupted once the suspension reached a final pH between 7 and 7.5, to prevent excessive acid input that could destabilize carbonate phases and increase the mobility of certain heavy metals within the carbonated IBA matrix.

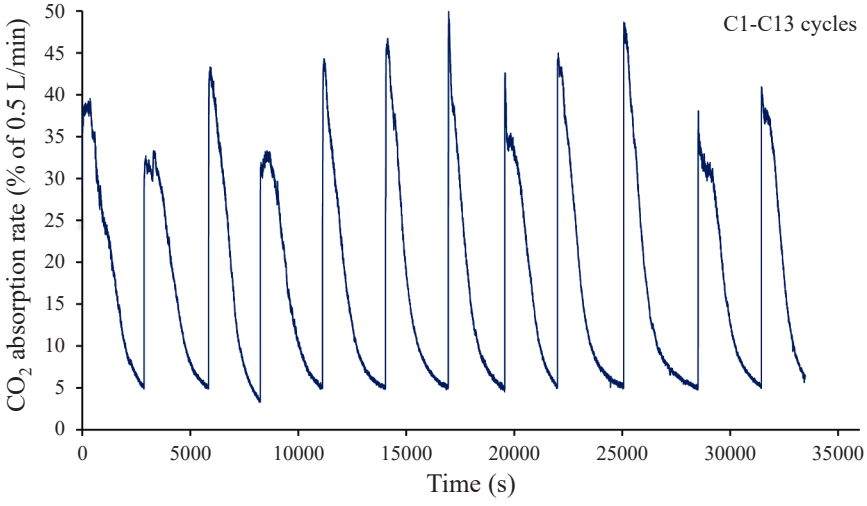

Fig. 7. CO_2 absorption rate η(t) across the thirteen cycles (experiment identifiers: C1–C13).

Table 3
Mean absorption rate $\overline{\eta}(t)$, maximum absorption rate $\eta(t)_{max}$ with standard deviation σ, carbonation step duration, volumetric CO_2 uptake V_{CO2}, carbonation degree achieved ω, final EC and pH for each cycle of the C1-C13 series. Note that in each cycle a fresh raw sample of IBA ultrafines is used, whereas the carbonating solution of cycle *n* corresponds to the wastewater recovered from cycle *n–1*.

Experiment Identifier	$\overline{\eta}(t)$ %	$\eta_{max}(t)$ %	σ	Duration s	V_{CO2} L	ω g/kg_{IBA}
C1	20.1	39.5	11.6	2856	5.24	118.7
C2	17.7	33.3	10.2	2985	4.83	108.1
C3	19.1	43.3	13.5	2398	4.18	91.2
C4	17.3	33.3	10.3	2877	4.55	100.9
C5	16.7	44.3	12.1	2920	4.46	98.4
C6	17.0	46.7	13.1	2904	4.51	99.7
C7	16.8	51.3	12.5	2616	4.00	86.7
C8	19.3	42.6	11.3	2437	4.29	94.1
C9	16.9	45.0	12.9	3068	4.72	105.2
C10	15.8	48.6	13.1	3452	4.97	111.7
C11	16.9	38.1	10.4	2924	4.50	99.6
C12	18.4	40.9	12.4	2510	4.21	92.1
C13	17.3	37.6	11.1	2689	4.24	92.9
Average	17.6	41.9	11.9	2818	4.51	99.9

Across the 13 cycles, the mean volumetric CO_2 uptake amounted to ~4.5 L, corresponding to a mean carbonation degree of ~100 gCO_2/kg of IBA.

Using IBA, carbonation studies in the literature typically report CO_2 uptakes ranging from ~25–45 gCO_2/kg and up to ~100–102 gCO_2/kg under optimized accelerated carbonation protocols, depending on ash particle size, freshness, and processing method (Lin et al., 2015; Chang et al., 2015; Lombardi et al., 2016; Brück et al., 2018a, 2018b, 2019a, 2019b; Steketee and Langevoort, 2020; Schnabel et al., 2021; Julcour et al., 2025; Qian et al., 2025; Fan and Zhang, 2025). The ~100 gCO_2/kg observed in this study is likely due to several factors: the abundance of reactive phases in the ultrafines, fresh sampling, an optimized reactor design with an effective porous stone sparger combined with mechanical stirring, and a high L/S ratio (10) promoting rapid and extensive dissolution and reprecipitation into $CaCO_3$.

3.2.2. Chemical evolution of the carbonation wastewaters

Fig. 8 shows the evolution of wastewater chemistry and pH/EC across the carbonation cycles for the major anions and trace metals. Supplementary Table S5 reports the detailed supernatant recovery results for C1–C13. Supernatant recovery remained highly consistent across cycles, with 868–897 g of water retrieved per run and a mean loss of 12.0 wt%, corresponding to a recovery efficiency of 88% per cycle. This limited loss indicates that the process operates with low water consumption, requiring only minor makeup additions to sustain closed-loop carbonation over multiple cycles.

However, the progressive reuse of the carbonation wastewater leads to a marked enrichment of dissolved species throughout the 13 cycles. The pH remains near-neutral (7.1–7.8), while EC increases steadily from 7 to 25 mS/cm, reflecting the accumulation of dissolved ions. Chloride and sulfate both exhibit increasing trends, with chloride rising from ~0.7 to ~5.1 g/L and sulfate from 1.3 to 3.0–3.6 g/L, after which both anions show a clear attenuation and approach stable, asymptotic concentrations. This plateau is consistent with the solution approaching (super)saturation, leading to the precipitation of solubility-controlling secondary phases such as gypsum or anhydrite in the case of sulfate. Fluoride remains undetected in the wastewaters at every carbonation stage.

Furthermore, most trace metals also show clear upward trends with increasing cycle number. Cu rises from 0.3 to 2.3 ppm, Sb from 360 to 685 ppb, Fe from 1.5 to 8.8 ppm, Mn from 0.16 to 1.3 ppm, Co from 8 to 57 ppb, Ni from 53 to 278 ppb, Cd from 1.5 to 24 ppb and Zn from 1.5 to 6.7 ppm. Arsenic (As) increases from 34 to 206 ppb. Pb remains low (< 10 ppb) in most cycles but exhibits episodic peaks reaching up to 126 ppb. Surprisingly, Cr is the only trace metal displaying a decreasing trajectory, falling from 0.87 to 1.3 ppm in the first eight cycles to 0.49–0.75 ppm in the last five cycles.

Overall, carbonation under wastewater reuse conditions results in a systematic accumulation of major anions and trace metals in the wastewater, progressively modifying the chemical environment of subsequent carbonation cycles. The contrasting behaviour of Cr relative to all other elements indicates that salinity, redox conditions and secondary mineral formation evolution throughout the cycles progressively control Cr mobility. Importantly, the results show that the CO_2-induced decomposition of soluble phases promotes the transfer of PTEs into the aqueous phase, where they can be readily removed from the IBA through the washing and solid–liquid filtration steps. This extraction mechanism provides a means to prevent their long-term release from the final carbonated product, thereby strengthening the overall environmental performance of the carbonation washing process.

3.3. Physicochemical characterization of the carbonated IBA

3.3.1. Morphology, microstructure, and microanalysis

Fig. 9 shows the widespread precipitation of calcite onto silicate grains in the carbonated IBA. The precipitated calcium carbonate (PCC) occurs as micron-sized rhombohedral calcite crystals, abundantly distributed as surface coatings or aggregates across the sample. This observation is consistent with the XRPD-detected increase in calcite peak intensity during carbonation (Fig. 6b). In

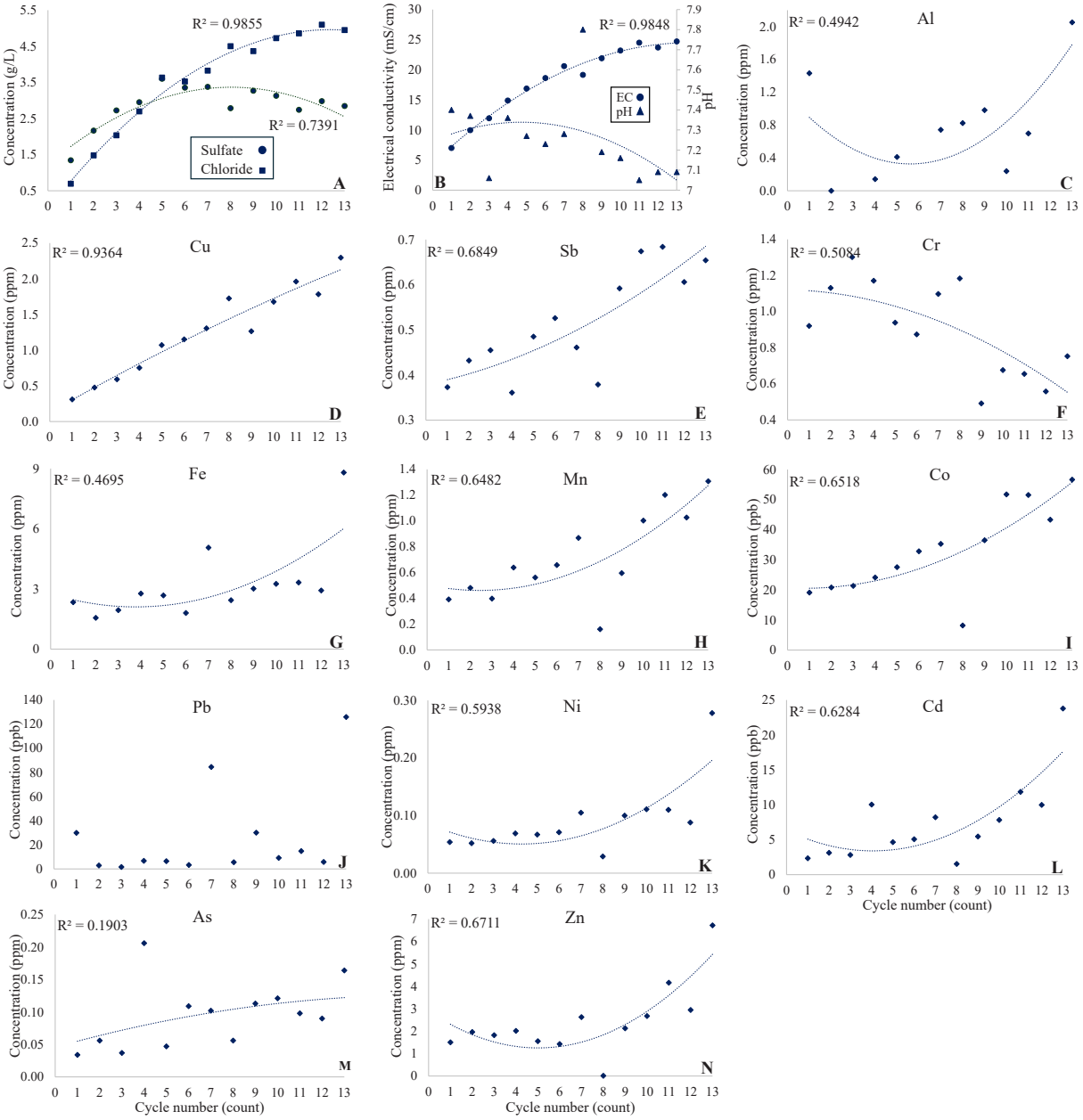

Fig. 8. Wastewater (C1–C13) PTEs concentrations and pH/EC as a function of the cycle number for: (A) sulfate and chloride, (B) EC/pH, (C) aluminum, (D) copper, (E) antimony, (F) chromium, (G) iron, (H) manganese, (I) cobalt, (J) lead, (K) nickel, (L) cadmium, (M) arsenic, and (N) zinc.

Fig. 8a, a dense assemblage of PCC is observed on a Ca–Mg silicate of åkermanite-like composition, whereas Fig. 8b shows a less dense but still evident PCC deposit on a Ca–Al silicate of gehlenite-like composition.

The presence of micron-sized rhombohedral calcite indicates carbonation under conditions of high aqueous supersaturation with respect to $CaCO_3$. As reported by Fan (Fan and Zhang, 2025), wet carbonation routes favour dissolution–reprecipitation reactions while largely preserving particle size, unlike semi-dry configurations that promote interparticle binding and agglomeration. In this study, the high L/S and efficient CO_2 dispersion through micro-bubbles enhanced gas–liquid mass transfer and Ca release, maintaining elevated calcite supersaturation. These conditions favour calcite nucleation in suspension rather than the formation and growth of interparticle carbonate bridges.

3.3.2. Mineralogical and chemical evolution across cycles

The thirteen XRPD patterns of the carbonated samples (Fig. 10) exhibit consistent mineralogical features, with calcite systematically emerging as the dominant crystalline phase and showing increased peak intensity relative to the pre-carbonation patterns, while

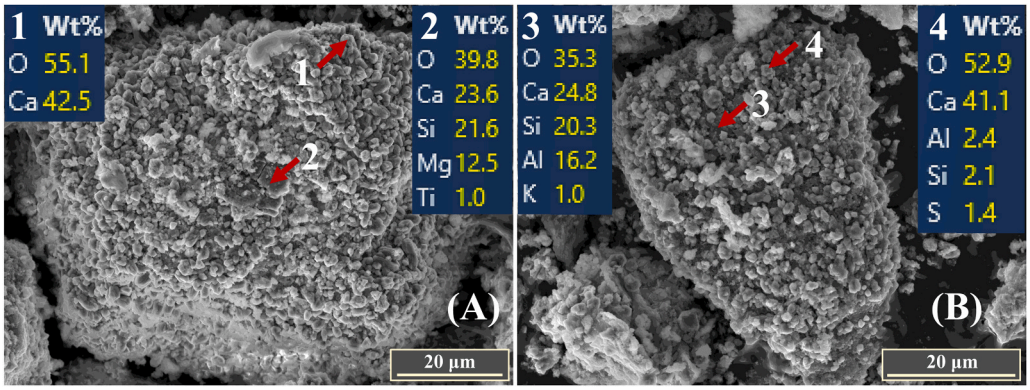

Fig. 9. SEM–EDS images of characteristic phases and minerals identified in the carbonated IBA. (A) Precipitated calcium carbonate (calcite) deposited on a mixed Ca–Mg silicate of åkermanite-like composition. (B) Precipitated calcium carbonate deposited on a Ca–Al silicate of gehlenite-like composition.

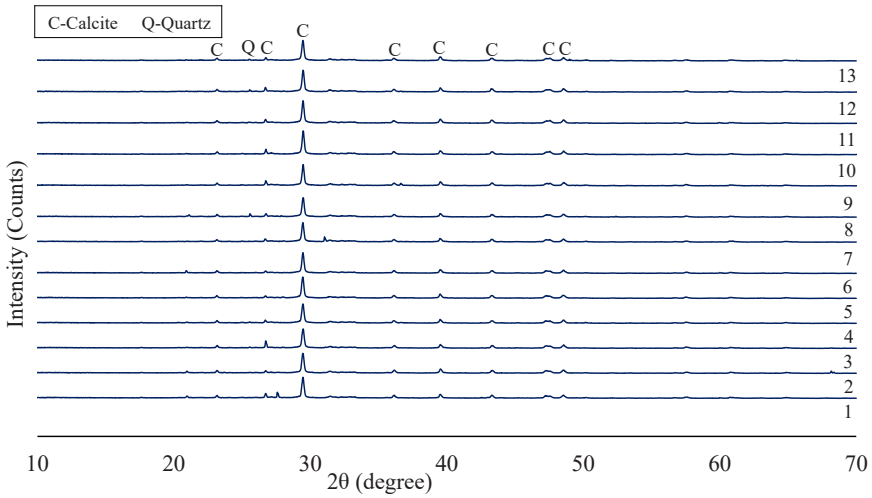

Fig. 10. Evolution of XRPD patterns of the carbonated samples over the thirteen successive carbonation cycles (C1–C13). The diffractograms highlight the persistence of calcite (C) as the dominant crystalline phase throughout the series, together with minor quartz (Q).

quartz is consistently detected as a minor component. This enhancement is accompanied by the disappearance of Hcl and Lrn peaks. The high consistency in peak positions and relative intensities indicates a stable mineralogical assemblage across cycles, suggesting that the accumulation of salts and PTEs during repeated carbonation washing steps does not induce significant changes in the crystalline phases formed. This mineralogical stability across cycles aligns with the chemical trends reported in Table 4, which summarizes the oxide composition (XRF) and LOI of the carbonated products. Notably, carbonation washing markedly reduced the concentrations of soluble and mobile components: Cl decreased by 80%, SO_3 by 43%, Na_2O by 52%, and K_2O by 29%. Concentrations of several heavy metals also decreased noticeably during carbonation washing. NiO decreased by 44% and PbO by 28%. However, with increasing carbonation washing cycles, the concentrations of these oxides progressively rise, yet remain consistently below pre-carbonation values. Cl increases from 0.29 to 0.76 wt%, SO_3 from 1.90 to 2.70 wt%, Na_2O from 0.63 to 0.93 wt%, and K_2O from 0.54 to 0.66 wt%. Similarly, PbO rises from 0.033 to 0.049 wt% and NiO from 0.009 to 0.015 wt%. This trend likely results from the combined effects of increasing PTEs concentrations in the residual wastewater retained after filtration and the progressive accumulation of PTEs in the recirculated wastewater. As cycles proceed, the reduced solid–liquid concentration gradient limits further PTEs release from the IBA ultrafines, thereby constraining the separation efficiency of carbonation washing.

3.3.3. Leaching behaviour of the carbonated samples

Fig. 6 presents the leaching behaviour of the carbonated IBA samples (A1 to A13) as a function of cycle number. Each cycle corresponds to a carbonation experiment carried out with recycled wastewater from the previous run so that the liquid phase becomes progressively more saline and enriched in dissolved metals, which in turn affects the composition of the leachates from the subsequently carbonated solids.

Table 4
XRF chemical composition (wt% of oxides) and loss on ignition (LOI) (wt%) of the carbonated samples across cycles. Chloride (Cl) is also included, expressed in atomic form.

	Cycle number												
Oxide	1	2	3	4	5	6	7	8	9	10	11	12	13
Na_2O	0.63	0.70	0.74	0.77	0.81	0.84	0.89	0.91	0.89	0.93	0.98	0.84	0.93
MgO	2.08	1.98	2.04	2.29	1.87	1.81	2.04	2.28	1.99	1.94	2.01	1.90	2.25
Al_2O_3	14.22	13.30	12.88	13.70	13.59	13.44	13.07	13.12	12.67	12.71	12.87	12.57	13.15
SiO_2	12.01	11.17	11.42	11.23	10.72	10.68	11.07	11.50	11.41	11.05	11.23	10.82	11.35
P_2O5	2.19	2.08	1.99	2.09	2.05	2.03	2.06	2.13	2.08	2.11	2.08	2.05	2.17
SO_3	1.90	2.35	2.46	2.48	2.47	2.42	2.66	2.56	2.55	2.53	2.60	2.62	2.70
Cl	0.29	0.34	0.44	0.49	0.50	0.62	0.64	0.67	0.70	0.63	0.72	0.71	0.76
K_2O	0.54	0.52	0.57	0.60	0.58	0.64	0.64	0.66	0.66	0.61	0.67	0.63	0.66
CaO	32.19	32.32	32.45	31.97	33.07	32.59	33.05	31.95	32.44	32.10	32.07	32.20	32.31
TiO_2	1.08	1.07	1.21	1.11	1.14	1.07	1.18	1.10	1.19	1.11	1.19	1.18	1.20
Cr_2O_3	0.075	0.062	0.088	0.059	0.073	0.047	0.066	0.074	0.084	0.073	0.062	0.053	0.069
MnO	0.099	0.099	0.104	0.087	0.080	0.091	0.096	0.074	0.093	0.095	0.098	0.084	0.101
Fe_2O_3	2.20	2.08	2.26	2.28	2.19	2.24	2.24	2.18	2.44	2.31	2.32	2.21	2.44
Co_2O_3	0.008	0.004	0.013	0.005	0.006	0.005	0.008	n.d.	n.d.	0.008	0.007	0.002	0.010
NiO	0.009	0.009	0.008	0.007	0.014	0.012	0.010	n.d.	0.011	0.012	0.012	0.012	0.015
CuO	0.155	0.150	0.162	0.161	0.148	0.154	0.153	0.163	0.169	0.156	0.171	0.160	0.158
ZnO	0.545	0.519	0.551	0.481	0.435	0.453	0.481	0.492	0.478	0.492	0.509	0.475	0.501
As_2O_3	n.d.	n.d.	n.d.	n.d.	n.d.	n.d.	n.d.	n.d.	n.d.	n.d.	n.d.	0.001	n.d.
Rb_2O	n.d.	n.d.	n.d.	0.004	n.d.	0.002	0.001	n.d.	n.d.	n.d.	n.d.	0.003	0.004
SrO	0.068	0.071	0.067	0.068	0.067	0.068	0.070	0.067	0.067	0.066	0.068	0.068	0.065
Y_2O_3	n.d.	n.d.	n.d.	0.002	n.d.	0.002	n.d.	n.d.	n.d.	n.d.	n.d.	0.000	n.d.
ZrO_2	0.014	0.011	0.014	0.012	0.015	0.009	0.011	0.026	0.012	0.015	0.014	0.012	0.014
BaO	0.195	0.191	0.177	0.159	0.163	0.145	0.052	0.190	0.194	0.187	0.151	0.151	0.165
PbO	0.033	0.031	0.029	0.039	0.029	0.034	0.037	0.037	0.044	0.043	0.045	0.049	0.041
CeO_2	n.d.	n.d.	n.d.	n.d.	0.011	n.d.	n.d.	n.d.	n.d.	n.d.	n.d.	n.d.	n.d.
V_2O5	n.d.	0.021	n.d.	0.019	n.d.	0.062	n.d.	n.d.	n.d.	n.d.	0.027	0.004	0.021
SnO_2	0.039	n.d.	0.033	0.037	0.014	n.d.	0.023	n.d.	n.d.	n.d.	n.d.	n.d.	n.d.
LOI	29.40	30.92	30.30	29.86	29.95	30.55	29.45	29.83	29.84	30.83	30.10	31.21	28.90

After the first carbonation step, leaching shows a marked reduction for most parameters compared to pre-carbonation levels (Fig. 6, red triangles), with EC decreasing by 64.9%, Al by 90.1%, Mn by 63.6%, Co by 83.8%, Ni by 84.8%, Cu by 93.2%, As by 67.0%, Cd by 70.7%, Pb by 95.6%, F^- by 70.1%, and Cl^- by 78.2% compared to the raw sample. Conversely, a limited number of elements exhibit increased leaching, with Cr, Fe, Sb, and SO_4^{2-} rising by 16.1%, 84.3%, 171.3%, and 107.6%, respectively, relative to the raw sample. These increases are primarily attributed to the carbonation-induced more acidic pHs (from 11.42 to ~7–8) and to the decomposition of reactive mineral phases, including Ca-aluminate surface coatings and sulfate-bearing phases such as ettringite.

Marked reductions in the leaching of divalent metal cations following mineral carbonation are widely documented, particularly for Cu, Zn, Pb, and Cd (Meima et al., 2002; Van Gerven et al., 2005; Arickx et al., 2010; Kim et al., 2023; Sun et al., 2024).

Furthermore, the overall solution chemistry of the carbonated samples clearly reflects the cumulative effect of wastewater recycling. Electrical conductivity increases from 1.3 to 3 mS/cm by cycle 13, while pH values range in 8.8–9.5. Chloride and sulfate concentrations follow a similar trend, increasing from 120 to 485 mg/L and from 390 to 673 mg/L, respectively. This progressive enrichment is consistent with the well-established release of chloride and sulfate during carbonation of IBA, resulting from the CO_2-driven decomposition of Hcl, Ett and AFm-type minerals (Um, 2019; Simon and Scholz, 2023; Lapp et al., 2025).

Al, As, Cd, Co, Cu, Fe, Ni and Pb also display a strong positive correlation between leaching concentration and cycle number. Al increases from ~3 to ~19 ppm; Cu from ~0.06 to ~0.22 ppm; Fe from ~0.2 to ~0.5 ppm; Co from ~0.1 to ~0.44 ppb; Ni from ~1 to ~10 ppb; Cd from ~0.07 to ~0.35 ppb; As from ~3 to ~12 ppb; and Pb from ~0.04 to ~2.5 ppb. Zn remains undetected in all leachates. Despite these increasing trends, all these metals remain below the regulatory limits after 13 cycles. Mn and Co remain at very low concentrations throughout all cycles, ranging from 0 to 10 ppb and from 0.1 to 3 ppb, respectively.

Conversely, Sb concentrations lie within a narrow range of ~80–110 μg/L and significantly exceed the regulatory limit (60 μg/L), consistent with the well-documented mobilization of Sb during IBA carbonation (Cornelis et al., 2006, 2012). This behaviour can be attributed to the predominance of Sb(V) oxyanions (e.g., $Sb(OH)_6^-$), which are weakly retained by mineral phases and highly sensitive to changes in pH and mineral assemblage. Carbonation induces the dissolution and transformation of reactive Ca- and Al-bearing phases, thereby reducing Sb retention and promoting its release into solution. From a practical perspective, Sb remains a key compliance-limiting element for IBA reuse, despite the overall improvement in leaching behaviour. However, this hypothesis is largely based on geochemical modelling and experimental simulations, including tests in which Ca- and Fe-containing additives were used to immobilize Sb, with interpretations relying primarily on total Sb concentrations measured in leachates by ICP-MS (Van Caneghem et al., 2016; Verbinnen et al., 2017). More broadly, Sb speciation in IBA remains insufficiently constrained, as most studies infer its occurrence indirectly from leaching behaviour and thermodynamic considerations rather than direct mineralogical identification (Blanc et al., 2018; Cornelis et al., 2011; Wehrung et al., 2024c).

Fluoride also falls below the regulatory limits, though increasing from 0.55 to 2.6 mg/L.

Consistent with the trend observed in the carbonation wastewaters, Cr is the only element exhibiting a significant decreasing trend, declining from ~260 to ~135 ppb and remaining apparently below the Type 1 threshold from cycle 8 onward. The decreasing trend observed after repeated carbonation under wastewater reuse conditions suggests that the process promotes a progressive immobilization of Cr. Several mechanisms could contribute, including partial reduction of Cr(VI) to the less soluble Cr(III) at the lower pH of the carbonated system, enhanced incorporation of Cr into newly formed Fe-rich phases as dissolved Fe increases, or co-precipitation with secondary solubility-controlling (hydr)oxides (Montesinos et al., 2014; Delina et al., 2025).

Taken together, these results show that operating carbonation washing under wastewater reuse conditions induces a progressive build-up of salts and several trace metals in the system, while critical elements such as Cr can instead be progressively stabilised. This contrasted behaviour indicates that closed-loop carbonation washing influences not only the magnitude but also the speciation and partitioning of redox-sensitive elements, with potentially beneficial effects for Cr. It also underscores the need to consider cycle number and wastewater management when evaluating the environmental performance of IBA carbonation processes.

The complexity of the mechanisms governing this process is reflected in the irregular evolution of the leaching trends as a function of the cycle number. This behaviour is ascribable to from several concurrent factors: (i) the dynamic equilibrium between leached species and their concentrations in the aqueous phase, whose composition progressively evolves with wastewater reuse; (ii) the occurrence of competing reactions, such as $Ca^{2+} + CO_3^{2-} \rightarrow CaCO_3$ and $Ca^{2+} + SO_4^{2-} \rightarrow CaSO_4$, resulting in competition between carbonate and sulfate anions for divalent counter-ions, like calcium and other cations; (iii) solution-mediated redox reactions leading to changes in oxidation state and precipitation of less soluble phases, as illustrated by the reduction of Cr(VI) to Cr(III). A systematically increasing leaching trend with cycle number indicates progressive saturation of the carbonating solution in a given species. This in turn leads to a gradual decrease in washing efficiency.

3.4. System-level integration and economic outlook

3.4.1. Integration of carbonation washing into an advanced IBA fines processing train

The results presented above suggest that carbonation washing could serve as a process building block for the treatment of IBA fines. The method achieves simultaneous CO_2 mineralization, initial PTE stabilization, and sustained performance across cycles, demonstrating that fine fractions can be made compatible with reuse scenarios if properly integrated into a broader treatment chain. To unlock full-scale feasibility and maximize resource recovery, carbonation washing should be embedded in an integrated process combining fine-fraction partitioning, enhanced metal recovery (EMR), optimized carbonation washing, efficient solid–liquid separation, targeted polishing of recirculated process waters, and tailored aggregate manufacturing.

Accordingly, Fig. 11 illustrates the proposed process workflow for the low-carbon recycling of the IBA ultrafine fraction, integrating carbonation washing within the upstream and downstream processing steps. The system proposed herein comprises:

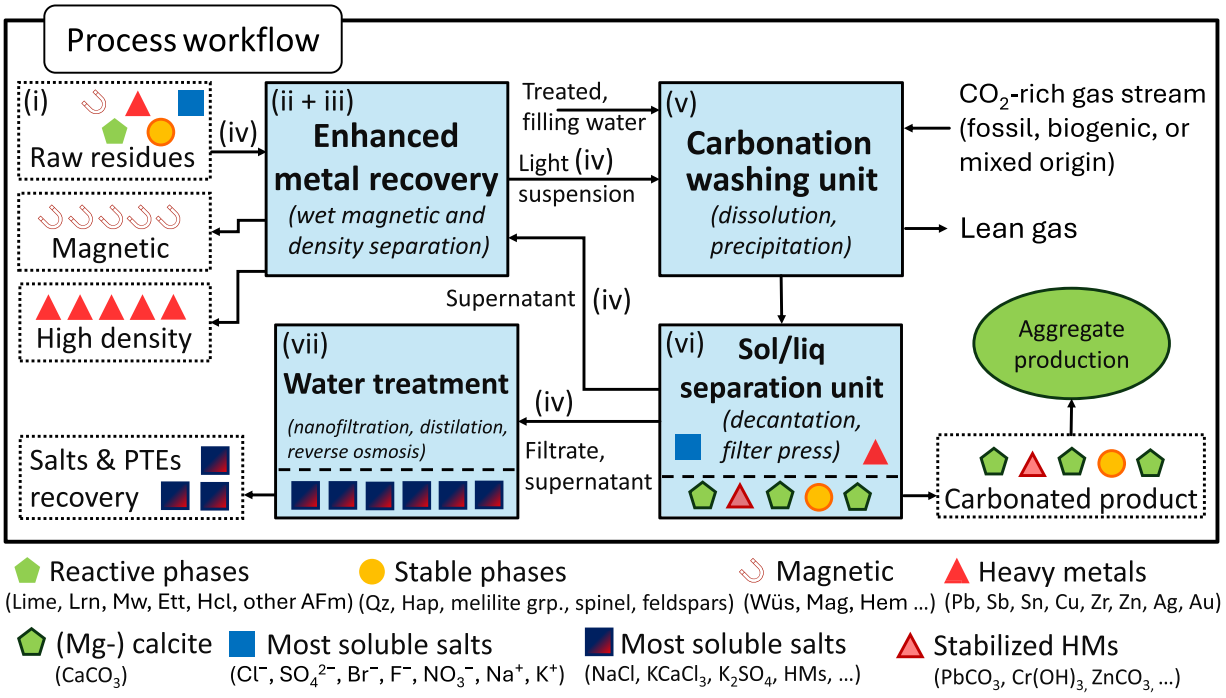

Fig. 11. Simplified schematic diagram of the proposed process workflow for low-carbon recycling strategy of IBA fine fractions under wastewater reuse and regeneration conditions.

(i) a mixing tank configured to receive a raw feedstock and recycled process water;
(ii) a magnetic separation unit configured to operate with recycled process water;
(iii) a density-based separation unit;
(iv) a material transfer unit;
(v) a carbonation unit comprising at least one carbonation reactor, configured with a water inlet and at least one CO_2 injection zone;
(vi) a solid–liquid separation unit, optionally comprising a settling tank and/or a mechanical dewatering system such as a filter press;
(vii) a water treatment unit configured to produce recycled process water directed to the mixing tank and/or the magnetic separation unit and/or the carbonation unit.
(viii) an aggregate production unit, enabling the conversion of treated and carbonated fine fractions into value-added materials such as lightweight aggregates or cementitious products.

From a resource-recovery perspective, (ultra)fine fractions (< 0.25–2 mm) should become explicit targets for EMR, since they host most leachable heavy metals and fine precious metals. Wet magnetic and density-based separation techniques, such as low-intensity magnetic separation (LIMS) and gravity or centrifugal separation, respectively, offer proven scalability. Technologies such as wet shaking tables and Falcon UF centrifugal concentration can separate metal-rich particles before carbonation, with the dual benefit of preventing downstream leaching and enabling strategic, critical and precious metal recycling (Kroll-Rabotin et al., 2012; Dehaine et al., 2019; Farajzadeh and Chelgani, 2022; Sierra et al., 2024; Mika et al., 2025). However, EMR cannot achieve complete heavy-metal removal, as a fraction of metals remains associated with oxide-bound phases and micro- to submicron-sized metal-bearing particles that persist in the medium-density tailings.

Furthermore, by reducing residual moisture and enabling in-press cake washing, press filtration can limit the carryover of soluble species, thereby enhancing product stability. However, due to the high abundance of submicron particles in the ultrafine fraction, the use of flocculation–agglomeration agents is required to achieve efficient press filtration.

In addition, carbonation washing under wastewater reuse leads to predictable enrichment of major anions and trace elements in the process water. This enables the design of targeted water-management strategies, including selective ion removal (e.g., sulfate or chloride), and polishing treatments such as adsorption, membrane-based separation (e.g., nanofiltration and reverse osmosis), or thermal processes (e.g., low-pressure distillation). Integrating such control steps will be essential for scaling closed-loop systems while limiting water consumption and complying with environmental reuse or discharge criteria.

Finally, beyond stabilization and metal recovery, the treated and carbonated fine fractions can be further valorized through aggregate production and incorporation into cementitious systems. In particular, the combination of carbonation-induced mineral transformations and controlled washing creates favourable conditions for the development of sustainable lightweight aggregates via granulation technologies (Tang et al., 2019; Quina et al., 2020; Caprai et al., 2020; Jin et al., 2024a, 2024b), as well as their integration into cementitious composites such as aerated mortars (Fan et al., 2022; Liu et al., 2024a, 2025; Brossat et al., 2024). The reduction of soluble salts and the partial stabilization of potentially toxic elements contribute to improving compatibility with binder systems, while the formation of carbonate phases can enhance material stability and long-term performance. In addition, solidification and encapsulation mechanisms within cementitious matrices can effectively immobilize residual heavy metals, substantially reducing their leaching potential and improving environmental compliance, as increasingly demonstrated in recent studies on IBA valorization (Yuan et al., 2023; Liu et al., 2024b).

In this context, the present process provides a complementary upstream treatment strategy, enabling the generation of more stable feedstocks tailored for these applications. Further work is required to optimize formulation, mechanical performance, and durability, but these results highlight the strong potential for integrating carbonation washing into circular construction-material value chains.

3.4.2. Preliminary techno-economic assessment and deployment scenarios

A preliminary techno-economic assessment was performed for an integrated IBA fine-treatment platform combining advanced physical separation, aqueous mineral carbonation, and water treatment under recirculation. While the estimate remains pre-design (Class 4/5 level), it provides order-of-magnitude constraints on scale, dominant cost drivers, and the key parameters controlling economic viability.

The estimated CAPEX is strongly capacity-dependent and increases with plant size due to (i) the multiplication and/or upscaling of solid handling units, (ii) utilities and instrumentation requirements, and (iii) civil works and integration constraints. For platforms treating $>$ 20,000 t IBA per year, total CAPEX can readily exceed €1 Million.

Across plausible configurations, CAPEX is primarily driven by the advanced physical separation train, which typically includes:

- Size classification (screens/sieves; possible de-agglomeration depending on feed moisture and fines cohesion),
- Solid–solid separation devices (magnetic separation and density-based units),
- Solid–liquid separation units (e.g., filter press and ancillary thickening/settling capacity).

The mineral carbonation and water-loop hardware (reactors, mixing tanks/reservoirs, CO_2 injection and distribution components, valves, pumps, piping manifolds, containers/skids, instrumentation and control, and the water treatment system enabling recycle) completes the equipment scope. The engineering and project delivery package (mechanical, electrical, and process engineering; integration; commissioning and start-up) constitutes a non-negligible fraction of total CAPEX and should be explicitly accounted for,

particularly given the hybrid nature of the projected platform (solids processing, wet chemistry, water treatment).

The OPEX distribution indicates that operating costs are dominated by labor and water/waste management, while electricity and CO_2 supply remain secondary but non-trivial contributors. A representative OPEX breakdown is as follows:

- Operators (31%)
- Waste & water treatment (20%)
- Operation & maintenance (13%)
- bioCO_2 sourcing (12%)
- Loading/handling (8%)
- Electricity (6%)
- Certification of CDR credits (4%)
- Administration and other costs (4%)
- Water consumption (1%)

This distribution highlights two engineering implications: (i) water-loop design and treatment robustness are central to economic performance (not only to environmental performance), and (ii) automation and process stability (reducing labor intensity and downtime) can materially shift OPEX.

Projected revenues are primarily controlled by non-ferrous metal recovery, which constitutes the main income stream (~63%). CDR credits contribute a substantial but secondary share (~22%), while treated mineral fraction valorization completes the revenue panel (~15%).

Consequently, economic performance is highly sensitive to metal recovery effectiveness, which itself depends on:

- initial grade in the fines (Cu, Zn, Pb, Sn, Ni as major base metals),
- liberation and partitioning of metal-bearing phases (size, morphology, association with glass/silicates/oxides),
- recoverability under the chosen separation route (magnetic and density separation performance; potential need for additional unit operations),
- the presence and potential upgrading of strategic/critical metals (e.g., Sb, Zr) and precious metals (Au, Ag), which can disproportionately influence the value of concentrates if recovery and refining routes exist.

In this context, the plant's business case is not governed solely by average bulk composition, but rather by the presence and recoverability of high-value particles and mineral phases, as well as by the ability of the process to generate saleable concentrates meeting impurity constraints and downstream smelter specifications. This makes robust monitoring of composition and recovery rates decisive for process margins.

Under the considered assumptions, the payback period is estimated to range between ~6 and 10 years, reflecting the strong combined sensitivity to throughput, metal revenues, and water/waste treatment costs.

Importantly, both statistical analyses and techno-economic assessments reported in the literature indicate that a minimum throughput on the order of ~20,000 t IBA per year is generally required to achieve positive economic indicators for IBA management pathways (Bruno et al., 2021; Chuchro et al., 2025). This threshold is typically discussed for the bulk IBA stream, whereas the present case study focuses on the fine fraction, which has a distinct composition, higher reactivity, and often higher metal enrichment but also higher handling and treatment constraints.

In France, the WtE landscape combines a limited number of large facilities with a majority of smaller plants distributed across the territory. This configuration naturally favors a deployment model where regional hubs provide the throughput required for cost-effective operation, especially when local reuse outlets exist for the demetallized mineral fraction.

From an engineering and project-finance standpoint, costs can be reduced materially when projects:

- are implemented on existing platforms with recoverable utilities, buildings, and land, or as retrofitting add-ons
- leverage pre-existing logistics and massification infrastructure (receiving, storage, internal handling, traffic management),
- are deployed during contract renewals or tender cycles.

Finally, early-stage feasibility must include a realistic mapping of outlets for each generated stream: metal concentrates, salt-rich residues/brines, and treated mineral fraction, with clear specifications, acceptance criteria, and logistics. In particular, the development of local metal refining pathways, currently limited or non-existent in France for bottom ash-derived non-ferrous streams, could improve both environmental and economic performance by reducing transport.

4. Conclusions

This study investigates carbonation washing applied to the ultrafine fraction of incineration bottom ash (IBA < 0.25 mm), which largely governs bulk IBA leaching behaviour. By coupling repeated carbonation cycles with wastewater reuse, the work provides a quantitative assessment of leaching evolution, CO_2 capture, and water-loop robustness, with direct implications for industrial deployment.

- A single carbonation washing step induces a strong decrease in leaching for most regulated elements (up to −95% for Pb, −93% for Cu, −85% for Ni, −71% for Cd, −67% for As and −78% for Cl^- relative to the raw ultrafine fraction). With increasing cycle number, partial re-enrichment occurs due to solute accumulation in the recirculated wastewater; nevertheless, after 13 cycles all metals except Sb remain below French Type 1 and Type 2 reuse thresholds. Cr exhibits a distinct behaviour, with leaching decreasing across cycles and falling below the Type 1 limit from cycle 8 onward.
- These results must be interpreted conservatively, as the investigated < 0.25 mm fraction is significantly finer and more reactive than the < 4 mm fraction for which Type 1 and Type 2 thresholds are defined. Achieving near-compliance for this isolated ultrafine fraction therefore represents a worst-case scenario, and reintegration into coarser matrices or cementitious systems is expected to further dilute leaching contributions.
- The process achieves a mean CO_2 uptake on the order of gCO_2 per kg of IBA, with uptake and carbonation efficiency remaining stable over 13 reuse cycles, indicating that increasing salinity and metal accumulation do not hinder carbonation performance.
- Carbonation washing was operated under a wastewater reuse conditions with an optimisable water recovery efficiency of approximately 88% per cycle. Major anions and trace metals accumulate in the recycled water but approach asymptotic concentrations controlled by secondary phase precipitation, enabling stable operating conditions.

- From a system perspective, carbonation washing simultaneously enables CO_2 mineralisation, contaminant transfer to the aqueous phase, and solid stabilisation.
- In industrial practice, ultrafines (∼15 wt% of IBA) dominate leaching and salt release; their targeted treatment therefore enables more efficient stabilisation and resource recovery compared to bulk processing.

Overall, carbonation washing can contribute to transforming IBA ultrafines from a leaching-critical fraction into a stable, CO_2-storing mineral feedstock. This requires integration into advanced treatment trains combining fine-fraction separation, metal recovery, efficient solid–liquid separation, and controlled water-loop management. increased mobility of specific species (e.g., Sb and SO_4^{2-}) highlights the need for further process optimisation.

Abbreviations

ACT	Accelerated Carbonation Technology
APCr	Air Pollution Control residues
IBA	Incineration Bottom Ash
EC	Electrical Conductivity
EDXS	Energy Dispersive X-ray Spectroscopy
EMR	Enhanced Metal Recovery
Ett	Ettringite
FA	Fly Ash
Hap	Hydroxylapatite
Hcl	Hydrocalumite
Hem	Hematite
HM(s)	Heavy Metal(s)
IAW	Industrial Alkaline Waste
IC	Ion Chromatography
ICP-MS	Inductively Coupled Plasma Mass Spectrometry
kgw	Kilogram of water
L/S	Liquid-to-Solid ratio
LIMS	low-intensity magnetic separation
Lrn	Larnite
Mag	Magnetite
MSW	Municipal Solid Waste
Mw	Merwinite
PCC	Precipitated Calcium Carbonate
ppt	parts per thousand
ppb	parts per billion
ppm	parts per million
SEM	Scanning Electron Microscope
Wüs	Wüstite
XRPD	X-ray Powder Diffraction

CRediT authorship contribution statement

Fabien Michel: Writing – review & editing, Visualization, Validation, Supervision, Resources, Project administration, Funding acquisition, Conceptualization. **Salah Mezlini:** Writing – review & editing, Visualization, Validation, Supervision, Project administration. **Linda Pastero:** Writing – review & editing, Visualization, Validation, Supervision, Software, Resources, Project administration, Methodology, Funding acquisition, Conceptualization. **Meissem Mezni:** Writing – review & editing, Writing – original draft, Visualization, Validation, Investigation, Formal analysis, Data curation. **Alessandro Pavese:** Writing – review & editing, Visualization, Validation, Supervision, Software, Resources, Project administration, Methodology, Investigation, Funding acquisition, Formal

analysis. **Nadia Curetti:** Writing – review & editing, Visualization, Validation, Formal analysis, Data curation. **Caterina Caviglia:** Writing – review & editing, Visualization, Validation, Formal analysis, Data curation. **Giovanna Antonella Dino:** Writing – review & editing, Visualization, Validation, Resources. **Federico Pasero:** Writing – review & editing, Visualization, Validation, Formal analysis, Data curation. **Enrico Destefanis:** Writing – review & editing, Visualization, Validation, Supervision, Resources, Project administration, Investigation, Formal analysis. **Davide Bernasconi:** Writing – review & editing, Writing – original draft, Methodology, Investigation, Formal analysis, Data curation. **Quentin Wehrung:** Writing – review & editing, Writing – original draft, Visualization, Validation, Supervision, Software, Resources, Project administration, Methodology, Investigation, Funding acquisition, Formal analysis, Data curation, Conceptualization.

Funding

This research was supported by Bpifrance through the award of a Bourse French Tech Emergence (BFTE) grant to the ASHES academia–industry program, "Aide à l'innovation", N°672550, led by Quentin Wehrung for Alkaline Technologies, at the Earth Sciences Department, University of Turin.

Declaration of Competing Interest

Quentin Wehrung and Fabien Michel are employees of Alkaline Technologies. The paper reflects the views of the scientists and not the company. The remaining authors declare that the research was conducted in the absence of any commercial or financial relationships that could be construed as a potential conflict of interest.

Appendix A. Supporting information

Supplementary data associated with this article can be found in the online version at doi:10.1016/j.eti.2026.104943.

Data Availability

Data will be made available on request.

References

AFNOR, «Caractérisation des déchets - Lixiviation - Essai de conformité pour lixiviation des déchets fragmentés, des boues - Partie 2: essai en bâchée unique avec un rapport liquide-solide de 10 l/kg, une granularité inférieure à 4 mm, Paris, 2002.

Alam, Q., Florea, M.V.A., Schollbach, K., Brouwers, H.J.H., 2017. A two-stage treatment for Municipal Solid Waste Incineration (MSWI) bottom ash to remove agglomerated fine particles and leachable contaminants. Waste Manag. 67, 181–192.

Alam, Q., Schollbach, K., van Hoek, C., van der Laan, S., de Wolf, T., Brouwers, H.J.H., 2019a. In-depth mineralogical quantification of MSWI bottom ash phases and their association with potentially toxic elements. Waste Manag. 87, 1–12.

Alam, Q., Schollbach, K., Rijnders, M., van Hoek, C., van der Laan, S., Brouwers, H.J.H., 2019b. The immobilization of potentially toxic elements due to incineration and weathering of bottom ash fines. J. Hazard. Mater. 379, 120798.

Alam, Q., Lazaro, A., Schollbach, K., Brouwers, H.J.H., 2020. Chemical speciation, distribution and leaching behavior of chlorides from municipal solid waste incineration bottom ash. Chemosphere 241, 124985.

Allegrini, E., Maresca, A., Olsson, M.E., Holtze, M.S., Boldrin, A., Astrup, T.F., 2014. Quantification of the resource recovery potential of municipal solid waste incineration bottom ashes. Waste Manag. 34 (9), 1627–1636.

Arickx, S., Borger, V.De, Van Gerven, T., Vandecasteele, C., 2010. Effect of carbonation on the leaching of organic carbon and of copper from MSWI bottom ash. Waste Manag. 30 (7), 1296–1302.

Asal, S., Laux, S.J., McVay, M.C., Townsend, T.G., 2019. Blending organic material with municipal solid waste incinerator bottom ash to promote in-situ carbonation in road base. Waste Manag. & Res. 37 (9), 951–955.

Baciocchi, R., Costa, G., Lategano, E., Marini, C., Polettini, A., Pomi, R., Rocca, S., 2010. Accelerated carbonation of different size fractions of bottom ash from RDF incineration. Waste Manag. 30 (7), 1310–1317.

Bansal, D., Gupta, G., Ramana, G.V., Datta, M., 2024. Optimizing MSW incineration bottom ash reuse: A study on treated wastewater washing and leaching control. Waste Manag. 182, 164–174.

Bayuseno, A.P., Schmahl, W.W., 2010. Understanding the chemical and mineralogical properties of the inorganic portion of MSWI bottom ash. Waste Manag. 230 (8-9), 1509–1520.

Beikmohammadi, M., Yaghmaeian, K., Nabizadeh, R., Mahvi, A.H., 2023. Analysis of heavy metal, rare, precious, and metallic element content in bottom ash from municipal solid waste incineration in Tehran based on particle size. Sci. Rep. 13 (1), 16044.

Bernasconi, D., Caviglia, C., Destefanis, E., Bonadiman, C., Brombin, V., Mancinelli, M., Pavese, A., 2025. Steam washing for MSWI-FA treatment. Waste Manag. 195, 10–21.

Beylot, A., Muller, S., Descat, M., Ménard, Y., Villeneuve, J., 2018. Life cycle assessment of the French municipal solid waste incineration sector. Waste Manag. 80, 144–153.

Blanc, D., Gonzalez, L., Lupsea-Toader, M., de Brauer, C., 2018. Mineralogical evolution and leaching behaviour of a heap of bottom ash as a function of time: influence on its valorization. Waste Biomass-.-. Valoriz. 9 (12), 2517–2527.

Blasenbauer, D., Huber, F., Lederer, J., Quina, M.J., Blanc-Biscarat, D., Bogush, A., Fellner, J., 2020. Legal situation and current practice of waste incineration bottom ash utilisation in Europe. Waste Manag. 102, 868–883.

Brossat, M., Prud'Homme, E., Lupsea-Toader, M., Blanc, D., de Brauer, C., 2024. Characterization of lightweight aerated mortars using waste-to-energy bottom ash (WtE-BA) as aerating agent. J. Environ. Manag. 356, 120443.

Brück, F., Schnabel, K., Mansfeldt, T., Weigand, H., 2018b. Accelerated carbonation of waste incinerator bottom ash in a rotating drum batch reactor. J. Environ. Chem. Eng. 6 (4), 5259–5268.

Brück, F., Fröhlich, C., Mansfeldt, T., Weigand, H., 2018a. A fast and simple method to monitor carbonation of MSWI bottom ash under static and dynamic conditions. Waste Manag. 78, 588–594.
Brück, F., Ufer, K., Mansfeldt, T., Weigand, H., 2019b. Continuous-feed carbonation of waste incinerator bottom ash in a rotating drum reactor. Waste Manag. 99, 135–145.
Brück, F., Mansfeldt, T., Weig, H., 2019a. Flow-through carbonation of waste incinerator bottom ash in a rotating drum batch reactor: Role of specific CO2 supply, mixing tools and fill level. J. Environ. Chem. Eng. 7 (2), 102975.
Bruno, M., Abis, M., Kuchta, K., Simon, F.G., Grönholm, R., Hoppe, M., Fiore, S., 2021. Material flow, economic and environmental assessment of municipal solid waste incineration bottom ash recycling potential in Europe. J. Clean. Prod. 2317, 128511.
Buchholz, B.A., Landsberger, S., 1995. Leaching dynamics studies of municipal solid waste incinerator ash. J. Air & Waste Manag. Assoc. 45 (8), 579–590.
Caprai, V., Schollbach, K., Florea, M.V.A., Brouwers, H.J.H., 2020. Investigation of the hydrothermal treatment for maximizing the MSWI bottom ash content in fine lightweight aggregates. Constr. Build. Mater. 230, 116947.
Caviglia, C., Confalonieri, G., Corazzari, I., Destefanis, E., Mandrone, G., Pastero, L., Pavese, A., 2019. Effects of particle size on properties and thermal inertization of bottom ashes (MSW of Turin's incinerator). Waste Manag. 84, 340–354.
Caviglia, C., Destefanis, E., Pastero, L., Bernasconi, D., Bonadiman, C., Pavese, A., 2022. MSWI fly ash multiple washing: Kinetics of dissolution in water, as function of time, temperature and dilution. Minerals 12 (6), 742.
Chang, E.E., Pan, S.Y.Y.L., Chen, Y.H., Kim, H., Chiang, P.C., 2015. Accelerated carbonation using municipal solid waste incinerator bottom ash and cold-rolling wastewater: Performance evaluation and reaction kinetics. Waste Manag. 43, 283–292.
Chen, Z., Li, J.S., Xuan, D., Poon, C.S., Huang, X., 2023. Effect of alkaline washing treatment on leaching behavior of municipal solid waste incineration bottom ash. Environ. Sci. Pollut. Res. 30 (1), 1966–1978.
Cheng, Y., Li, Z., Zhang, P., Chen, J., Qin, C., 2025. CO2 mineralization and heavy metal leaching of multi-source ashes from municipal solid waste incineration. Sep. Purif. Technol. 354, 128825.
Chrysochoou, M., Dermatas, D., 2006. Evaluation of ettringite and hydrocalumite formation for heavy metal immobilization: Literature review and experimental study. J. Hazard. Mater. 136, 20–33.
Chuchro, M., Jędrusiak, R., Bielowicz, B., 2025. Statistical analyses of precious metal contents in waste incineration bottom ashes. Sci. Rep. 15 (1), 8149.
Cornelis, G., Van Gerven, T., Vandecasteele, C., 2006. Antimony leaching from uncarbonated and carbonated MSWI bottom ash. J. Hazard. Mater. 137 (3), 1284–1292.
Cornelis, G., Johnson, C.A., Gerven, T.Van, Vandecasteele, C., 2008. Leaching mechanisms of oxyanionic metalloid and metal species in alkaline solid wastes: A review. Appl. Geochem. 23 (5), 955–976.
Cornelis, G., Gerven, T.Van, Snellings, R., Verbinnen, B., Elsen, J., Vandecasteele, C., 2011. Stability of pyrochlores in alkaline matrices: solubility of calcium antimonate. Appl. Geochem. 26 (5), 809–817.
Cornelis, G., Gerven, T.Van, Vandecasteele, C., 2012. Antimony leaching from MSWI bottom ash: modelling of the effect of pH and carbonation. Waste Manag. 32 (2), 278–286.
Dehaine, Q., Foucaud, Y., Kroll-Rabotin, J.S., Filippov, L.O., 2019. Experimental investigation into the kinetics of Falcon UF concentration: Implications for fluid dynamic-based modelling. Sep. Purif. Technol. 215, 590–601.
Delina, R.E., Perez, J.P.H., Roddatis, V.V., Stammeier, J.A., Prieur, D., Scheinost, A.C., Tan, M.M., Garcia J. J. L, A.C.A., Benning, L.G., 2025. Immobilization of Chromium by Iron Oxides in Nickel–Cobalt Laterite Mine Tailings. Environ. Sci. & Technol. 59 (11), 5683–5692.
Destefanis, E., Caviglia, C., Bernasconi, D., Bicchi, E., Boero, R., Bonadiman, C., Wehrung, Q., 2020. Valorization of MSWI bottom ash as a function of particle size distribution, using steam washing. Sustainability 12 (22), 9461.
Di Gianfilippo, M., Costa, G., Verginelli, I., Gavasci, R., Lombardi, F., 2016. Analysis and interpretation of the leaching behaviour of waste thermal treatment bottom ash by batch and column tests. Waste Manag. 56, 216–228.
Di Gianfilippo, M., Hyks, J., Verginelli, I., Costa, G., Hjelmar, O., Lombardi, F., 2018. Leaching behaviour of incineration bottom ash in a reuse scenario: 12 years-field data vs. lab test results. Waste Manag. 73, 367–380.
L.M. Directeur général de la prévention des risques, «Arrêté du 18 novembre 2011 relatif au recyclage en technique routière des mâchefers d'incinération de déchets non dangereux modifié par,» 2011.
Dong, J., Tang, Y., Nzihou, A., Chi, Y., Weiss-Hortala, E., Ni, M., Zhou, Z., 2018. Comparison of waste-to-energy technologies of gasification and incineration using life cycle assessment: Case studies in Finland, France and China. J. Clean. Prod. 203, 287–300.
Dou, X., Ren, F., Nguyen, M.Q., Ahamed, A., Yin, K., Chan, W.P., Chang, V.W.C., 2017. Review of MSWI bottom ash utilization from perspectives of collective characterization, treatment and existing application. Renew. Sustain. Energy Rev. 79, 24–38.
Fan, X., Zhang, D., 2025. Unveiling the Role of Processing Route in CO2 Mineralization by Incineration Bottom Ash under Near-Ambient Aqueous Conditions. Environ. Sci. & Technol. Lett. 12 (3), 341–347.
Fan, X., Li, Z., Zhang, W., Jin, H., Chen, C., Liu, J., Xing, F., Tang, L., 2022. Effects of different supplementary cementitious materials on the performance and environment of eco-friendly mortar prepared from waste incineration bottom ash. Constr. Build. Mater. 356, 129277.
Farajzadeh, S., Chelgani, S.Chehreh, 2022. Gravity separation by falcon concentrator-an over review. Sep. Sci. Technol. 57 (13), 2145–2164.
Fletcher, C.A., Dunk, R., 2023. Recovery and utilisation of municipal solid waste incineration bottom ash: implications for European waste management strategy. Detritus 23, 43–57.
Gori, M., Pifferi, L., Sirini, P., 2011. Leaching behaviour of bottom ash from RDF high-temperature gasification plants. Waste Manag. 31 (7), 1514–1521.
Huber, F., Blasenbauer, D., Aschenbrenner, P., Fellner, J., 2019. Chemical composition and leachability of differently sized material fractions of municipal solid waste incineration bottom ash. Waste Manag. 95, 593–603.
Hyks, J., Šyc, M., Korotenko, E., Cajthaml, T., Semerád, J., Hjelmar, O., 2025. Leaching of per-and polyfluoroalkyl substances (PFAS) from municipal solid waste incineration bottom ash intended for utilization as secondary aggregates in road subbase. J. Hazard. Mater., 136635
Inkaew, K., Saffarzadeh, A., Shimaoka, T., 2016. Modeling the formation of the quench product in municipal solid waste incineration (MSWI) bottom ash. Waste Manag. 52, 159–168.
Jiang, Y., Ma, Z., Gu, Z., Liu, F., Shen, P., Poon, C.S., 2024. A novel approach for improving aqueous carbonation kinetics with CO2 micro-and nano-bubbles. Chem. Eng. J. 500, 157363.
Jin, H., Cheng, L., Liu, J., Chen, C., Xing, F., 2024b. Recycling and valorization of municipal solid waste incineration bottom ash via cold-bonded granulation technology–The role of fiber volume and fiber type. Constr. Build. Mater. 442, 137427.
Jin, H., Cheng, L., Liu, J., Chen, C., Xing, F., 2024a. Converting municipal solid waste incineration bottom ash into the value-added artificial lightweight aggregates through cold-bonded granulation technology. Constr. Build. Mater. 438, 136930.
Julcour, C., Dandach, A., Cassayre, L., Bourgeois, F., 2025. CO2 mineralization of bottom ash and decarbonation of waste-to-energy plants. J. CO2 Util. 99, 103169.
Kasina, M., Telk, A., Wendorff-Belon, M., 2024. Comprehensive characterization and environmental implications of industrial and hazardous incineration ashes: insights into chemistry, mineralogy, elements' fractionation and leaching potential. Sci. Rep. 14 (1), 29010.
Keber, S., Schirmer, T., Elwert, T., Goldmann, D., 2020. Characterization of fine fractions from the processing of municipal solid waste incinerator bottom ashes for the potential recovery of valuable metals. Minerals 10 (10), 838.
Kim, J.J., Lee, S.S., Fenter, P., Myneni, S.C., Nikitin, V., Peters, C.A., 2023. Carbonate coprecipitation for Cd and Zn treatment and evaluation of heavy metal stability under acidic conditions. Environ. Sci. & Technol. 57 (8), 3104–3113.
Kleib, J., Aouad, G., Abriak, N.E., Benzerzour, M., 2021. Production of Portland cement clinker from French municipal solid waste incineration bottom ash. Case Stud. Constr. Mater. 15, e00629.
Kroll-Rabotin, J.S., Bourgeois, F., Climent, É., 2012. Experimental validation of a fluid dynamics based model of the UF Falcon concentrator in the ultrafine range. Sep. Purif. Technol. 92, 129–135.

Lapp, F., Brück, F., Göske, J., Dohrmann, R., Mansfeldt, T., Weigand, H., 2025. Fresh and Aged Chromite Ore Processing Residues (COPR): Weathering-Induced Alteration of Chemical Properties, Cr (VI) Mobility and Mineralogy At Open Dumpsites in Kanpur, India. Water Air & Soil Pollut. 236 (2), 121.
Lin, W.Y., Heng, K.S., Sun, X., Wang, J.Y., 2015. Accelerated carbonation of different size fractions of MSW IBA and the effect on leaching. Waste Manag. 41, 75–84.
Liu, J., Wu, Y., Cheng, L., Jin, H., Li, J., Xing, F., 2024b. Assessment of mechanical and heavy metal leaching behavior of resource-efficient engineered cementitious composites incorporating ultra-high-volume municipal waste incineration bottom ash. J. Mater. Res. Technol. 33, 5784–5808.
Liu, J., Wu, Y., Cheng, L., Jin, H., Liu, J., Xing, F., 2024a. Recycling of municipal solid waste incineration bottom ash (MSWIBA) particles into natural fine sands for sustainable engineering cementitious composites. Constr. Build. Mater. 418, 135500.
Liu, J., Ren, Y., Cheng, L., Jin, H., Xing, F., 2025. Unlocking the potential of municipal solid waste incineration bottom ash into sustainable fine aggregates for production of eco-friendly lightweight sprayed mortar. J. Build. Eng. 108, 112880.
Loginova, E., Volkov, D.S., Van De Wouw, P.M.F., Florea, M.V.A., Brouwers, H.J.H., 2019. Detailed characterization of particle size fractions of municipal solid waste incineration bottom ash. J. Clean. Prod. 207, 866–874.
Lombardi, L., Carnevale, E.A., Pecorini, I., 2016. Experimental evaluation of two different types of reactors for CO2 removal from gaseous stream by bottom ash accelerated carbonation. Waste Manag. 58, 287–298.
Mantovani, L., Tribaudino, M., Matteis, C.D., Funari, V., 2021. Particle size and potential toxic element speciation in municipal solid waste incineration (MSWI) bottom ash. Sustainability 13 (4), 1911.
Mantovani, L., De Matteis, C., Tribaudino, M., Boschetti, T., Funari, V., Dinelli, E., Pelagatti, P., 2023. Grain size and mineralogical constraints on leaching in the bottom ashes from municipal solid waste incineration: a comparison of five plants in northern Italy. Front. Environ. Sci. 11, 1179272.
Matsumoto, H., Takaoka, M., 2021. Formation of Friedel's salt in simulated municipal solid waste incineration bottom ash. J. Mater. Cycles Waste Manag. 23 (4), 1374–1382.
Meima, J.A., van der Weijden, R.D., Eighmy, T.T., Comans, R.N., 2002. Carbonation processes in municipal solid waste incinerator bottom ash and their effect on the leaching of copper and molybdenum. Appl. Geochem. 17 (12), 1503–1513.
Mika, S., Mühl, J., Skutan, S., Aschenbrenner, P., Limbeck, A., Lederer, J., 2025. Substance flows of heavy metals in industrial-scale municipal solid waste incineration bottom ash treatment: A case study from Austria. Waste Manag. 195, 240–252.
Montesinos, V.N., Quici, N., Halac, E.B., Leyva, A.G., Custo, G., Bengio, S., Zampieri, G., Litter, M.I., 2014. Highly efficient removal of Cr (VI) from water with nanoparticulated zerovalent iron: Understanding the Fe (III)–Cr (III) passive outer layer structure. Chem. Eng. J. 244, 569–575.
Morf, L.S., Gloor, R., Haag, O., Haupt, M., Skutan, S., Lorenzo, F.Di, Böni, D., 2013. Precious metals and rare earth elements in municipal solid waste–sources and fate in a Swiss incineration plant. Waste Manag. 33 (3), 634–644.
Muchova, L., Bakker, E., Rem, P., 2009. Precious metals in municipal solid waste incineration bottom ash. Water Air & Soil Pollut. Focus 9, 107–116.
Nørgaard, K.P., Hyks, J., Mulvad, J.K., Frederiksen, J.O., Hjelmar, O., 2019. Optimizing large-scale ageing of municipal solid waste incinerator bottom ash prior to the advanced metal recovery: Phase I: Monitoring of temperature, moisture content, and CO2 level. Waste Manag. 85, 95–105.
Qian, J., Li, Z., Sun, J., Bao, S., Liu, F., Li, Y., Yang, L., 2025. Collaborative resource recovery and carbon emission reduction from municipal solid waste incineration bottom ash through semi-dry carbon sequestration. Process Saf. Environ. Prot. 12 (3), 108023.
Quina, M.J., Garcia, R., Simões, A.S., Quinta-Ferreira, R.M., 2020. Life cycle assessment of lightweight aggregates produced with ashes from municipal solid waste incineration. J. Mater. Cycles Waste Manag. 22, 1922–1931.
Renforth, P., 2019. The negative emission potential of alkaline materials. Nat. Commun. 10 (1), 1401.
Santos, R.M., Mertens, G., Salman, M., Cizer, Ö., Van Gerven, T., 2013. Comparative study of ageing, heat treatment and accelerated carbonation for stabilization of municipal solid waste incineration bottom ash in view of reducing regulated heavy metal/metalloid leaching. J. Environ. Manag. 128, 807–821.
Schnabel, K., Brück, F., Mansfeldt, T., Weigand, H., 2021. Full-scale accelerated carbonation of waste incinerator bottom ash under continuous-feed conditions. Waste Manag. 125, 40–48.
Shen, X., Liu, C., Zhao, Y., Li, Q., Wang, J., 2025. The recycling use of MSWI bottom ash as road construction material for carbon emissions reduction based on life cycle Assessment—a case study in China. Waste Manag. 207, 115122.
Sierra, H.M., Šyc, M., Korotenko, E., 2024. Wet shaking table operating parameters optimization for maximizing metal recovery from incineration bottom ash fine fraction. Waste Manag. 174, 539–548.
Simon, F.G., Scholz, P., 2023. Assessment of the Long-Term Leaching Behavior of Incineration Bottom Ash: A Study of Two Waste Incinerators in Germany. Appl. Sci. 13 (24), 13228.
Speiser, C., Baumann, T., Niessner, R., 2000. Morphological and chemical characterization of calcium-hydrate phases formed in alteration processes of deposited municipal solid waste incinerator bottom ash. Environ. Sci. & Technol. 34 (23), 50.
Spreadbury, C.J., McVay, M., Laux, S.J., Townsend, T.G., 2021. A field-scale evaluation of municipal solid waste incineration bottom ash as a road base material: Considerations for reuse practices. Resour. Conserv. Recycl. 168, 105264.
Steketee, J., Langevoort, M., 2020. Production of a stable building material by treatment of MSWI bottom ash with the Tauw EquiAsh® process. Waste Biomass-.-. Valoriz. 11 (12), 7109–7116.
Sun, X., Li, J., Zhao, X., Zhu, B., Zhang, G., 2016. A review on the management of municipal solid waste fly ash in American. Procedia Environ. Sci. 31, 535–540.
Sun, X., Xu, B., Yi, Y., 2024. Effects of accelerated carbonation on fine incineration bottom ash: CO2 uptake, strength improvement, densification, and heavy metal immobilization. J. Clean. Prod., 143714
Šyc, M., Simon, F.G., Hykš, J., Braga, R., Biganzoli, L., Costa, G., Grosso, M., 2020. Metal recovery from incineration bottom ash: State-of-the-art and recent developments. J. Hazard. Mater. 393, 122433.
Tang, P., Xuan, D., Poon, C.S., Tsang, D.C., 2019. Valorization of concrete slurry waste (CSW) and fine incineration bottom ash (IBA) into cold bonded lightweight aggregates (CBLAs): Feasibility and influence of binder types. J. Hazard. Mater. 368, 689–697.
Um, N., 2019. Effect of Cl removal in MSWI bottom ash via carbonation with CO2 and decomposition kinetics of Friedel's salt. Mater. Trans. 60 (5), 837–844.
Um, N., Nam, S.Y., Ahn, J.W., 2013. Effect of accelerated carbonation on the leaching behavior of Cr in municipal solid waste incinerator bottom ash and the carbonation kinetics. Mater. Trans. 54 (8), 1510–1516.
Van Caneghem, J., Verbinnen, B., Cornelis, G., de Wijs, J., Mulder, R., Billen, P., Vandecasteele, C., 2016. Immobilization of antimony in waste-to-energy bottom ash by addition of calcium and iron containing additives. Waste Manag. 54, 162–168.
Van Gerven, T., Van Keer, E., Arickx, S., Jaspers, M., Wauters, G., Vandecasteele, C., 2005. Carbonation of MSWI-bottom ash to decrease heavy metal leaching, in view of recycling. Waste Manag. 25 (3), 291–300.
Vehlow, J., Bergfeldt, B., Visser, R., Wilén, C., 2007. European Union waste management strategy and the importance of biogenic waste. J. Mater. Cycles Waste Manag. 9, 130–139.
Verbinnen, B., Van Caneghem, J., Billen, P., Vandecasteele, C., 2017. Long term leaching behavior of antimony from MSWI bottom ash: influence of mineral additives and of organic acids. Waste Biomass-.-. Valoriz. 8, 2545–2552.
Vogel, C., Scholz, P., Kalbe, U., Caliebe, W., Tayal, A., Vasala, S.J., Simon, F.G., 2024. Speciation of antimony and vanadium in municipal solid waste incineration ashes analyzed by XANES spectroscopy. J. Mater. Cycles Waste Manag. 1–7.
Wehrung, Q., Pastero, L., Bernasconi, D., Cotellucci, A., Bruno, M., Cavagna, S., Pavese, A., 2024b. Impact of Operational Parameters on the CO2 Absorption Rate in Ca(OH)2 Aqueous Carbonation— Implications for Process Efficiency. Energy & Fuels 38 (17), 16678–16691.
Wehrung, Q., Bernasconi, D., Cotellucci, A., Destefanis, E., Caviglia, C., Bicchi, E., Pavese, A., Pastero, L., 2024a. Carbonation washing of waste incinerator air pollution control residues under wastewater reuse conditions. J. Environ. Chem. Eng. 13 (1), 115272.
Wehrung, Q., Bernasconi, D., Destefanis, E., Caviglia, C., Curetti, N., Di Felice, S., Bicchi, E., Pavese, A., Pastero, L., 2024c. Aqueous Carbonation of Waste Incineration Residues: Comparing BA, FA, and APCr Across Production Scenarios. Minerals 14 (12), 1269.
Wehrung, Q., Bernasconi, D., Michel, F., Destefanis, E., Caviglia, C., Curetti, N., Pasero, F., Pavese, A., Pastero, L., 2025a. ASHES Program: An Academia-Industry Partnership Integrating Metal Recovery with Accelerated Carbonation from Fine Bottom Ashes Fractions. earthdoc 2025, 1–5.

Wehrung, Q., Bernasconi, D., Michel, F., Destefanis, E., Caviglia, C., Curetti, N., Mezni, M., Pavese, A., Pastero, L., 2025b. Accelerated Carbonation of Waste Incineration Residues: Reactor Design and Process Layout from Laboratory to Field Scales—A Review. Clean. Technol. 7 (3), 58.
Wei, Y., Shimaoka, T., Saffarzadeh, A., Takahashi, F., 2011. Mineralogical characterization of municipal solid waste incineration bottom ash with an emphasis on heavy metal-bearing phases. J. Hazard. Mater. 2187 (1-3), 534–543.
Xia, Y., He, P., Shao, L., Zhang, H., 2017. Metal distribution characteristic of MSWI bottom ash in view of metal recovery. J. Environ. Sci. 52, 178–189.
Yeo, R.J., Sng, A., Wang, C., Tao, L., Zhu, Q., Bu, J., 2024. Strategies for heavy metals immobilization in municipal solid waste incineration bottom ash: a critical review. Rev. Environ. Sci. Bio/Technol. 23 (2), 503–568.
Yin, K., Chan, W.P., Kumaran, S., Tamilselvam, O., Chen, W.Q., Latiff, N.B.M., Lisak, G., 2011. Redistribution of mineral phases of incineration bottom ash by size and magnetic separation and its effects on the leaching behaviors. Environ. Pollut. 290, 118015.
Yuan, Z., Cai, G., Gao, L., Wu, M., Kong, L., Bai, J., Li, W., 2023. The physical encapsulation and chemical fixation of Zn during thermal treatment process of municipal solid waste incineration (MSWI) fly ash. Waste Manag. 166, 203–210.
Zhang, J., Zhang, Y., Leong, Z.H., Zhang, Y., Chen, T., Fei, F., Wen, Z., 2025. Mapping the recycling potential of bottom ashes from waste-to-energy plants toward circular economy: evidence from China. Environ. Sci. & Technol. 59 (38), 20805–20816.
Zou, H., He, P., Lü, F., Zhang, H., 2025. Practice and challenges for beneficial use of municipal solid waste incineration bottom ash in China. J. Environ. Chem. Eng. 13 (5), 117923.